frontiers | Frontiers in Marine Science

TYPE Original Research
PUBLISHED 17 January 2024
DOI 10.3389/fmars.2023.1156918

OPEN ACCESS

EDITED BY
Stéphanie Dupré,
Institut Français de Recherche pour l'Exploitation de la Mer, France

REVIEWED BY
Hailin Yang,
Peking University, China
Thomas Pape,
University of Bremen, Germany

*CORRESPONDENCE
Ji-Hoon Kim
save@kigam.re.kr

†These authors have contributed equally to this work and share first authorship

RECEIVED 02 February 2023
ACCEPTED 26 December 2023
PUBLISHED 17 January 2024

CITATION
Kim J-H, Park M-H, Ryu J-S, Jang K, Choi J, Park S, Song Y, Yi B-Y, Joo YJ, Kim T-H and Hur J (2024) Exploring the pore fluid origin and methane-derived authigenic carbonate properties in response to changes in the methane flux at the southern Ulleung Basin, South Korea. *Front. Mar. Sci.* 10:1156918. doi: 10.3389/fmars.2023.1156918

Exploring the pore fluid origin and methane-derived authigenic carbonate properties in response to changes in the methane flux at the southern Ulleung Basin, South Korea

Ji-Hoon Kim[1*†], Myong-Ho Park[2†], Jong-Sik Ryu[3], Kwangchul Jang[4,5], Jiyoung Choi[1], Sanghee Park[6], Yungoo Song[5], Bo-Yeon Yi[1], Young Ji Joo[3], Tae-Hoon Kim[7] and Jin Hur[8]

[1]Marine Geology & Energy Division, Korea Institute of Geoscience and Mineral Resources, Daejeon, Republic of Korea, [2]Carbon Capture & Storage (CCS) Research Center, Kongju National University, Gongju, Republic of Korea, [3]Department of Earth and Environmental Sciences, Pukyong National University, Busan, Republic of Korea, [4]Division of Glacier Environment Research, Korea Polar Research Institute, Incheon, Republic of Korea, [5]Department of Earth System Sciences, Yonsei University, Seoul, Republic of Korea, [6]Division of Earth and Environment Sciences, Korea Basic Science Institute, Cheongju, Republic of Korea, [7]Geology & Space Division, Korea Institute of Geoscience and Mineral Resources, Daejeon, Republic of Korea, [8]Department of Environment & Energy, Sejong University, Seoul, Republic of Korea

We investigated the geochemistry of gas, pore fluid, and methane-derived authigenic carbonate (MDAC) from four sites in the southern Ulleung Basin, South Korea. In contrast to Sites 16GH-P1 and 16GH-P5, Sites 16GH-P3, and 16GH-P4 are characterized by acoustic chimney structures associated with gas flux. The composition of gas and isotopic signatures of methane (CH_4) (C_1/C_{2+} > 300, $\delta^{13}C_{CH4}$ < -60‰, δD_{CH4} ≤ -190‰) indicate microbial source CH_4 at all sites. The upward migration of CH_4 can affect the chemical and isotopic properties of pore fluid and gas-related byproducts (e.g., gas hydrate (GH) and MDAC) within the shallow sediments including the current sulfate-methane transition (SMT) (< 5 meters below seafloor). Although no GH was found, elevated Cl^- concentrations (maximum = 609 mM) with low δD and $\delta^{18}O$ values in Site 16GH-P4 pore fluids delineate the influence of massive GH formation in deeper sediment. In contrast, relatively constant Cl^-, δD, and $\delta^{18}O$ values in fluids from Sites 16GH-P1, 16GH-P3, and 16GH-P5 indicate a predominant origin from seawater. Pore fluids also exhibit higher concentrations of H_4SiO_4, B, Mg^{2+}, and K^+, along with increasing alkalinity compared to seawater. These observations suggest that marine silicate weathering alters fluid chemistry within the sediment, affecting element and carbon cycles. High alkalinity (up to 60 mM) and Mg^{2+}/Ca^{2+} ratios (> 6) alongside decreasing Ca^{2+} and Sr^{2+} concentrations imply carbonate precipitation. MDACs with diverse morphologies, mainly composed of aragonite and magnesian calcite, and characterized by low carbon isotopic values ($\delta^{13}C_{MDAC}$ < -31.3‰), were found at Sites 16GH-P3 and 16GH-P4. Interestingly, $\delta^{13}C_{MDAC}$ values at Site 16GH-P3 are clearly differentiated above and below the current SMT. High $\delta^{13}C_{MDAC}$ values

10.3389/fmars.2023.1156918

above the SMT (> -34.3‰) suggest the combined influence of seawater and CH_4 migrating upward on MDAC precipitation, whereas low $\delta^{13}C_{MDAC}$ values below it (< -41.6‰) indicate a predominant impact of CH_4 on MDAC formation. Additionally, the vertical variation of $\delta^{18}O_{MDAC}$ values at Site 16GH-P4, compared to the theoretical values, reflects an association with GH dissociation and formation. Our findings improve the understanding of fluid, gas, and MDAC geochemistry in continental margin cold seeps, providing insights into global carbon and element cycles.

KEYWORDS

microbial CO_2 reduction, marine silicate weathering, chimney structure, MDACs, gas hydrate, Ulleung Basin

1 Introduction

Cold seep systems that are characterized by the seepage of fluids enriched in methane (CH_4)-dominated hydrocarbons from deep-seated sediments to the seafloor under low temperatures, widely occur in many regions along the continental margin (e.g., Campbell, 2006; Judd and Hovland, 2007; Suess, 2014; Himmler et al., 2015; Mazzini et al., 2016). These systems play an important role in global climate change, element cycles, ocean chemistry, and biology (Dillon et al., 2001; Römer et al., 2014; Koch et al., 2015; Ruppel and Kessler, 2017). They also cause various changes in seafloor morphologies, for example, carbonate pavements, mounds, pockmarks, and mud volcanoes (Bahr et al., 2007; Buerk et al., 2010; Himmler et al., 2011; Römer et al., 2014; Koch et al., 2015). Geophysical investigations, for example, sub-bottom profiles, side scan sonar, and high-resolution seismic data, have been used to identify cold seep systems on the seafloor (e.g., Colbo et al., 2014; Stott et al., 2019; Böttner et al., 2020).

More than 80% of the CH_4 migrating upward below sulfate-methane transition (SMT) in sediments can be consumed via anaerobic oxidation of methane (AOM; Equation 1) mainly coupled with particulate organic carbon sulfate reduction (POCSR; Equation 2) in the SMT (Boetius et al., 2000; Peckmann and Thiel, 2004; Torres et al., 2020).

$$\mathrm{AOM}: CH_4 + SO_4^{2-} \rightarrow HCO_3^- + HS^- + H_2O \quad (1)$$

$$\mathrm{POCSR}: 2(CH_2O)_x(NH_3)_y(H_3PO_4)_z + xSO_4^{2-} \rightarrow xH_2S + 2xHCO_3^- + 2yNH_3 + 2zH_3PO_4 \quad (2)$$

where x, y, and z are derived from C:N:P ratios (Redfield ratios) of the organic matter.

These biogeochemical reactions provide energy for diverse chemosynthetic communities that colonize in the near-surface sediments of cold seeps (Sibuet and Olu, 1998). In addition, high HCO_3^- in pore fluid produced by the reactions provides favorable conditions for the precipitation of methane-derived authigenic carbonates (MDACs; Equation 3) in the sediment and/or water column, which is characterized by the low carbon isotopic value inherited from CH_4 (Peckmann et al., 2001; Luff et al., 2004; Torres et al., 2020). Gas hydrates (GHs) have also been found at cold seeps located in the Arctic regions, Cascadia Margin, and South China Sea (e.g., Han et al., 2008; Malinverno et al., 2008; Wang et al., 2014; Hong et al., 2017; Kim et al., 2020; Kim et al., 2022).

$$\mathrm{MDAC}: 2HCO_3^- + xCa^{2+} + (1-x)Mg^{2+} \rightarrow (Ca_x, Mg_{(1-x)})CO_3 + CO_2 + H_2O \quad (3)$$

where $x = Ca^{2+}/(Ca^{2+} + Mg^{2+})$.

Multichannel seismic investigations have been performed to find GHs in the Ulleung Basin, South Korea, since 2000. The prominent "chimney structures" (e.g., Figures 1B, D) frequently occur in this basin, which are characterized by seismic amplitude reduction resulting from velocity pull-up. These structures are associated with numerous fractures resembling hydrofractures and/or faults, terminating at different stratigraphic levels and, in some cases, extending to the seafloor (e.g., Lee et al., 2005; Haacke et al., 2009; Horozal et al., 2009; Ryu et al., 2009; Kim et al., 2012). Indeed, massive GHs have been found near the seafloor in the Ulleung Basin (e.g., Ryu et al., 2009; Kim et al., 2012; Choi et al., 2013; Kim et al., 2013), where a significant amount of free gas migrates upward from the deep-seated sediment via chimney structures forming GHs. Hence, these seismic structures potentially serve as pathways for the free gas migration feeding massive GH accumulations near the seafloor, which are unique seismic characteristics compared to other regions (e.g., Haacke et al., 2009; Horozal et al., 2009; Ryu et al., 2009; Kim et al., 2012; Choi et al., 2013; Kim et al., 2013; Hong et al., 2014). Many datasets (e.g., seismic survey, pore fluid chemistry, gas chemistry, and sedimentology) have been documented in the Ulleung Basin (e.g., Park et al., 2006; Park et al., 2007; Haacke et al., 2009; Kim et al., 2011; Kim et al., 2012; Choi et al., 2013; Kim et al., 2013), but

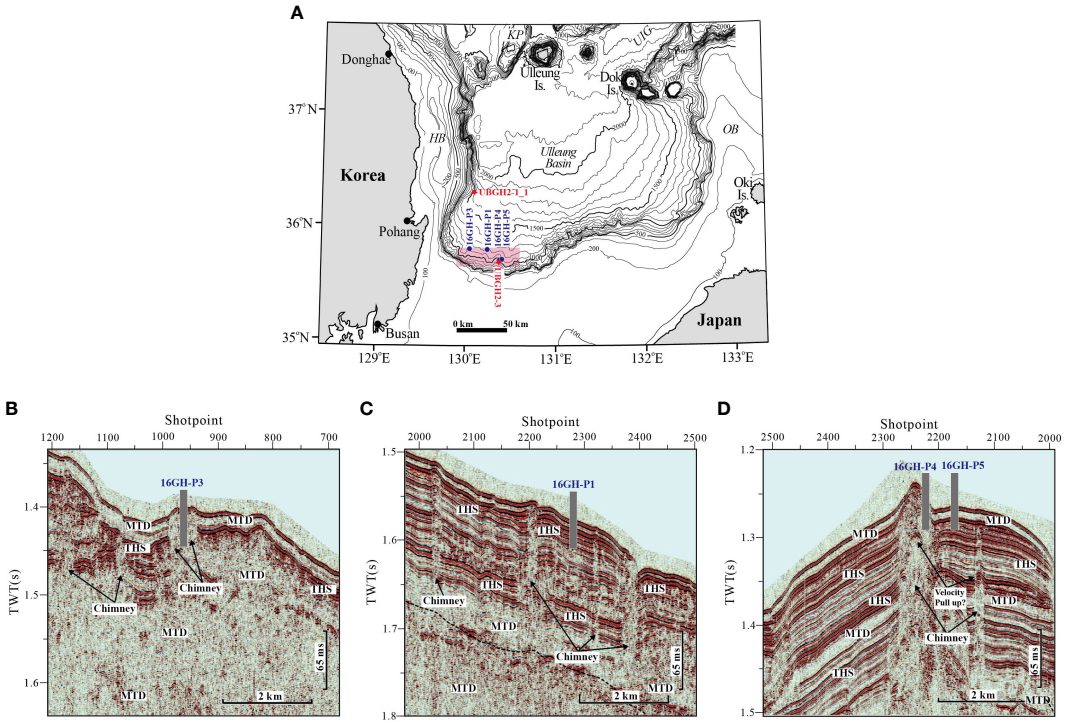

FIGURE 1
(A) Major physiographic features and locations of the study area (contour lines show the bathymetry in meters). KP, Korea Plateau; UIG, Ulleung Interplain Gap; HB, Hupo Bank, and OB, Oki Bank. Seismic profiles of **(B)** Site 16GH-P3 (chimney structure), **(C)** Site 16GH-P1 (non-chimney structure), and **(D)** Sites 16GH-P4 (chimney structure) and 16GH-P5 (non-chimney structure). The core depth at each site has no scale. MTD, mass-transport deposits and THS, turbidite-hemipelagic sediments.

studies for understanding the chemical interactions among gases, pore fluids, and sediments (including MDAC) are still rare in this basin.

In the present article, we investigated 1) how the upward migration of CH_4 from deep-seated sediments via chimney structures impacts the chemical properties of gases and fluids, as well as the characteristics of the shallow sedimentary deposits within the southern Ulleung Basin, and 2) how the petrological and morphological features of MDACs vary within the sediment column. To achieve our goals, we collected and conducted geochemical analysis for gases, pore fluids, and MDAC samples from two MDAC-bearing sites (16GH-P3 and 16GH-P4) and two non-MDAC-bearing sites (16GH-P1 and 16GH-P5).

2 Regional setting

The East Sea is the marginal sea in the northwestern Pacific Ocean and consists of three main basins (East Sea, Yamato, and Ulleung) and four straits (Korea, Tsugaru, Soya, and Tartar). The Ulleung Basin is bounded by the continental slope of the Korean Peninsula to the west and the Korea Plateau to the north and has a relatively steep gradient (up to 10°), while it is bordered by a rather gentle slope (1° ~ 2°) and a broad shelf (30 m ~ 50 km wide) of the Japanese Arc and the Oki Bank (Figure 1). This basin was formed during the late Oligocene to early Miocene by crustal extension (Tamaki et al., 1992; Jolivet et al., 1995).

The uppermost sedimentary sequence (30 m ~ 70 m thick) in the Ulleung Basin mainly consists of various mass-flow deposits along the entire margin of the basin overlain by Holocene hemipelagic mud (1 m ~ 2 m thick) (Chough et al., 2000; Lee et al., 2005). The average sedimentation rates of late Quaternary sediments in the basin range from 9 cm/ka to 20 cm/ka (Park et al., 2006; Park et al., 2007; Kim et al., 2011).

Sediment cores were collected at four sites on the slope of the southwestern part of the Ulleung Basin, ranging in water depth from 902 m to 1,187 m (Figure 1; Table 1). This region is characterized by prominent seafloor gullies due to numerous erosional slump events. The sedimentary deposits within the top 150 meters below seafloor (mbsf) consist mainly of turbidite and hemipelagic sequences that are parallel to the seafloor. Deeper layers are predominantly composed of mass transport deposits, with only a few coherent seismic reflection events discernible (Figures 1B–D). Among the sites, both Sites 16GH-P3 and 16GH-P4 display chimney structures with widths of approximately 600 m and 800 m, respectively, which show structural deformations within the sedimentary layers. However, a conspicuous bottom simulating reflector is not observed at the seismic section of these sites. In contrast, Sites 16GH-P1 and 16GH-P5 show non-chimney structures, which are well represented by the successive acoustic surfaces below the seafloor (Figure 1; Table 1) (KIGAM, 2016).

TABLE 1 Summaries of site information from the 2016 Expedition.

Site	Core	Latitude (°N)	Longitude (°E)	Water Depth (m)	Total Core Length (m)	SMT Depth (mbsf)	Seismic Characteristic	Remark
16GH-P3	16GH-P3*W	35.7681	130.0339	1,054	7.67	1.9	Chimney	***MDAC found
	16GH-P3*A	35.7683	130.0339	1,050	7.70	**——		
16GH-P4	16GH-P4W	35.6908	130.3433	916	6.95	2.5		MDAC not found
	16GH-P4A	35.6909	130.3403	902	7.70	——		MDAC found
16GH-P1	16GH-P1W	35.7992	130.2361	1,187	7.75	4.3	Non-chimney	MDAC not found
	16GH-P1A	35.7993	130.2361	1,187	7.48	——		
16GH-P5	16GH-P5W	35.6915	130.3503	926	7.10	2.7		
	16GH-P5A	35.6909	130.3498	925	7.47	——		

*W: core for geochemical study, A: core for sedimentological study.
**——: no data.
*** MDAC: methane-derived authigenic carbonate.

3 Materials and methods

3.1 Fluid sampling and analyses

Piston cores (PCs) were collected from four sites during the *R/V Tamhae II* cruise of the Korea Institute of Geoscience and Mineral Resources (KIGAM) in 2016. Two parallel PCs were sampled at each site for geochemical and sedimentological studies. These cores were designated as "W" and "A", corresponding to 16GH-P1W and 16GH-P1A, respectively (Table 1). Pore fluid was extracted by Rhizons throughout the whole round core of PC for geochemical analyses at approximately 40 cm ~ 85 cm intervals under 4°C. Extracted fluid was collected in an acid-prewashed syringe equipped with an in-line 0.20 µm disposable polytetrafluoroethylene filter. Fluid aliquots for cations and $^{87}Sr/^{86}Sr$ ratios were transferred into acid-prewashed high-density polyethylene (HDPE) bottles (~2 ml - 4 ml) and acidified with 20 µl ultrapure-grade HNO_3. Fluid subsamples for shipboard and anions analyses were collected in acid-prewashed HDPE bottles without acidification. Subsamples for stable isotopic compositions of water (δD and $\delta^{18}O$) and dissolved inorganic carbon ($\delta^{13}C_{DIC}$) were collected in 2 ml septum screw-lid glass vials. Fluid samples for $\delta^{13}C_{DIC}$ analysis were preserved with 30 µl $HgCl_2$. All fluid samples were stored at ~4°C in the refrigerator until the analyses.

Chlorinity (Cl^-) and alkalinity were analyzed onboard by titration with 0.1 M $AgNO_3$ and with 0.02 M HCl, respectively. The reproducibility of Cl^- and alkalinity was determined to be < 2% and < 0.5%, respectively, by repeated analysis of the International Association of Physical Sciences of the Oceans (IAPSO) standard seawater. Sulfate (SO_4^{2-}) was determined by Dionex ion chromatography (ICS-1100, Thermo Scientific) at the Korea Basic Science Institute (KBSI). IAPSO standard seawater was repeatedly measured to verify the analytical quality of the instruments, and analytical reproducibility was better than ±3%.

Major and minor cations (Na^+, K^+, Mg^{2+}, Ca^{2+}, Ba^{2+}, B, Sr^{2+}, and Si) were analyzed by PerkinElmer inductively coupled plasma-optical emission spectroscopy (Optima 8300 ICP-OES) at the KBSI. The reproducibility estimated from repeated analyses of reference materials (SLRS-5 and NASS-5) was < 5%.

Stable isotopic compositions of water (δD and $\delta^{18}O$) were analyzed by a VG Prism stable isotope ratio mass spectrometer (SIRMS) at the KBSI. The analytical reproducibility was ±1‰ for δD and ±0.1‰ for $\delta^{18}O$. $\delta^{13}C_{DIC}$ was determined with a Finnigan DELTA-Plus stable isotope ratio mass spectrometer using a Gas-Bench II automated sampler at the Oregon State University. The reproducibility was better than 0.07‰, based on the multiple standard measurements. Isotopic values are reported in the conventional δ-notation relative to Vienna Standard Mean Ocean Water (V-SMOW) for hydrogen and oxygen and Vienna Peedee Belemnite (V-PDB) for carbon.

Strontium (Sr) in the fluid was separated for $^{87}Sr/^{86}Sr$ analysis using Sr-Spec columns (Eichrom-Sr resin). The $^{87}Sr/^{86}Sr$ ratio was measured using a Neptune multi-collector inductively coupled plasma mass spectrometer (MC-ICP-MS, Thermo Finnigan) at the KBSI. The measured $^{87}Sr/^{86}Sr$ ratios were normalized to $^{86}Sr/^{88}Sr = 0.1194$, and repeated NBS 987 measurements yielded a value of 0.71025 ± 0.00002 ($2\sigma_{mean}$, $n = 24$).

3.2 Headspace gas sampling and analyses

Bulk sediments (3 ml) were sampled from the core to analyze the chemical compositions and isotopic ratios of headspace gas at approximately 40 cm ~ 82 cm intervals using a 5 ml cutoff plastic

syringe. The sediments were extruded into 20 ml serum glass vials, and 2 ml of saturated NaCl solution was added to them. The vials were immediately capped with rubber septa and sealed with aluminum crimp caps. Headspace gas was extracted by heating the sediment samples at 60°C for 30 minutes at the KIGAM, following the procedure described by Pimmel and Claypool (2001). Aliquot of the headspace gas sample was injected into an Agilent Technologies 7890A gas chromatography with both a flame ionization detector and a thermal conductivity detector to determine the hydrocarbon composition (C_1-C_6) and CO_2. The reproducibility was less than 3% based on repeated standard analyses.

The carbon and hydrogen stable isotopic compositions ($\delta^{13}C_{CH4}$, $\delta^{13}C_{CO2}$, and δD_{CH4}) in headspace gas samples were analyzed by a compound-specific isotope ratio-monitoring gas chromatography/mass spectrometer at Isotech Laboratories Inc. (Champaign, IL, USA). The carbon and hydrogen isotopic values are reported in the conventional δ-notation in permil (‰) relative to V-PDB and V-SMOW, respectively. The reproducibility of the analyses was ±0.1‰ for carbon and ±2‰ for hydrogen.

3.3 MDAC sampling and analyses

The cores for the sedimentological study were cut in the laboratory at KIGAM. One half of each core was preserved as an archived core and the other half was further processed as a working core. MDACs were hand-picked from the split cores of Sites16GH-P3 and 16GH-P4 at the KIGAM (Figure 2; Table 1). These samples were stored at approximately 4°C in the refrigerator until the analyses (< 3 months). Before analysis, the MDAC was washed repeatedly with Milli-Q water (resistivity of 18.2 MΩ·cm), and sonicated for a few minutes to eliminate adhered materials. It was washed again with Milli-Q water and dried at 60°C in an oven for 12 hours.

The thin sections of selected MDACs were observed using a polarization microscope (Nikon LV100N POL) at Yonsei University. The microstructure of the MDACs was examined on freshly fractured surfaces using a scanning electron microscope (SEM; JEOL JSM-5410) at Yonsei University.

For the analyses of bulk mineralogy and isotopic compositions ($\delta^{13}C$ and $\delta^{18}O$) of MDACs, the selected MDAC samples (> 20 g) were finely ground using a mortar and pestle and then thoroughly mixed for homogenization, following the method by Tong et al. (2019). In addition, the surface of the MDAC cutting prepared for the thin section shows little variation in texture and structure within each sample. As a result, the measured mineralogy and isotopic compositions represent the average of each MDAC sample. The bulk mineralogy and the relative abundance of carbonate minerals were determined through X-ray diffraction (XRD) using a Miniflex II XRD (RIGAKU) at Yonsei University. The ground MDAC

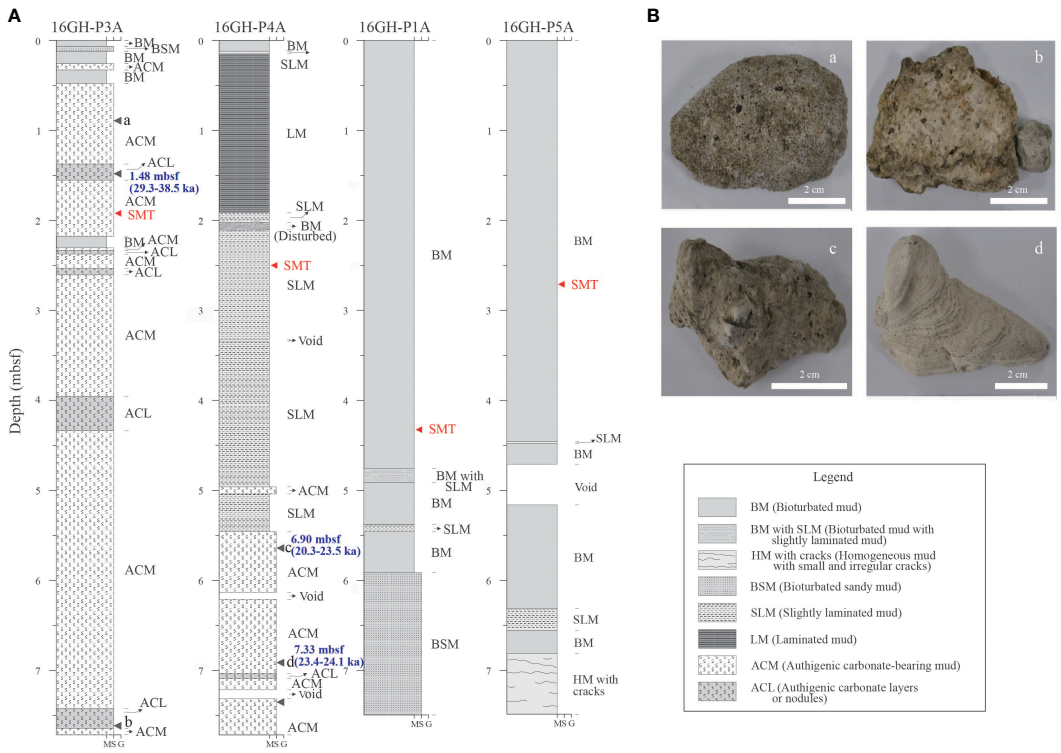

FIGURE 2
(A) Lithology of core sediment from Sites 16GH-P1, 16GH-P3, 16GH-P4, and 16GH-P5 in the southwestern part of the Ulleung Basin (mbsf: meters below seafloor). **(B)** Photographs of methane-derived authigenic carbonates (MDACs) from (a) 0.90 mbsf at Site 16GH-P3 (massive-porous type), (b) 7.69 mbsf at Site 16GH-P3 (semi-/un-consolidated type), (c) 5.70 mbsf at Site 16GH-P4 (massive-porous type), and (d) 6.90 mbsf at Site 16GH-P4 (massive-laminated type). The black closed arrows at Site 16GH-P3 and Site 16GH-P4 are core depths and ages of MDACs determined by U-Th dating, and the red closed arrow indicates the current SMT depth. The lithology description was used in the cores for sedimentological study at Sites 16GH-P1A, 16GH-P3A, 16GH-P4A, and 16GH-P5A. The M, S, and G in the X-axis of **(A)** are mud, sand, and gravel, respectively.

sample was thoroughly mixed homogeneously with corundum (Al_2O_3) powder in a 1:1 weight ratio. The XRD analysis was conducted on the powder samples under Cu-Kα radiation, utilizing a step-scan mode with 0.02° step, 1 sec/step scanning time, and 2° – 55° 2θ range. The analysis was performed using a 6-sample holder. Semi-quantitative analysis of mineral composition was conducted with the Reference Intensity Ratio (RIR) method (Hubbard et al., 1976; Hubbard and Snyder, 1988; Park et al., 2018). The ratio of peak intensities between corundum and major minerals was determined from the results of X-ray diffraction analysis. The quantitative values were then calculated based on the theoretical RIR values.

An aliquot of the bulk MDAC sample (~5 mg) from 0.90 mbsf to 7.69 mbsf at Site 16GH-P3 and from 5.70 mbsf to 7.33 mbsf at Site 16GH-P4 was reacted with 100% H_3PO_4 at 90°C for 5 minutes, and the evolved CO_2 gas was automatically injected into a VG Prism SIRMS in the KBSI for $\delta^{13}C$ and $\delta^{18}O$ analyses. The analytical reproducibility for $\delta^{13}C$ and $\delta^{18}O$ was < ± 0.1‰. Isotopic values are reported in the conventional δ-notation relative to V-PDB for carbon and oxygen.

Uranium (U)-thorium (Th) dating was performed at the NERC Isotope Geosciences Laboratory, British Geological Survey. Sample powders (1.6 mg ~ 8.9 mg) were drilled from 3 MDACs, which were from 3.30 mbsf at Site 16GH-P3, and 6.90 mbsf and 7.33 mbsf at Site 16GH-P4, using a hand-held microdrill. U and Th were separated, concentrated, and measured as described in Crémiere et al. (2016). These samples were dissolved in 8 M HNO_3 and then centrifuged to separate the soluble carbonate fraction from the insoluble detritus. The detritus was digested using a mixture of $HClO_4$:HF:HNO_3 (1:2:8 vol.), dried, and redissolved in 1 M HCl. U and Th were preconcentrated via iron co-precipitation and separated via column ion chromatography (Edwards et al., 1987). Isotope ratios were measured with an MC-ICP-MS (Thermo Finnigan). U-Th age calculations were carried out by the approach of Cheng et al. (2013), and a detrital correction was applied based on average measured $^{232}Th/^{238}U$, $^{230}Th/^{238}U$, and $^{234}U/^{238}U$ activity ratios of carbonate-free detritus samples from the Ulleung Basin.

4 Results

4.1 Sedimentary facies

Sediments in the cores are classified into eight sedimentary facies, mainly based on grain size, sedimentary structures, and distribution pattern of MDACs (Figure 2A). Among them, muddy sediments can be divided into six types: bioturbated mud (BM), bioturbated mud with slightly laminated mud (BM with SLM), homogeneous mud with small and irregular cracks (HM with cracks), bioturbated sandy mud (BSM), slightly laminated mud (SLM), and laminated mud (LM). Laminae are mostly less than a few mm thick and usually consist of coarser and finer (silt-clay) couplets in the LM interval, whereas they are not sharp and distinctly differentiated into coarse-fine couplets in the SLM interval. The BM facies is the most common mud facies in the upper part of the core from Sites 16GH-P1 and 16GH-P5 (non-chimney sites) and is characterized by various burrow structures, such as circular, oval, tubular, or irregular shapes. In contrast, the sediment from Sites 16GH-P3 and 16GH-P4 (chimney sites) is characterized by abundant MDACs in the mud facies (Figure 2A). These sedimentary facies with MDACs can be divided largely into two types: authigenic carbonate-bearing mud (ACM: mud with randomly scattered authigenic carbonate nodules) and authigenic carbonate layers or nodules (ACL) (Figure 2A).

4.2 Geochemical properties of pore fluids

The chemical properties of the pore fluids are shown in Figure 3 and Supplementary Table 1. The Cl^- concentration at all sites can be divided into two groups. The first group, found at Sites 16GH-P3 and 16GHP-P4 (chimney sites), shows a constant Cl^- concentration from the seafloor to 1.50 mbsf (~533 mM) and 0.78 mbsf (~552 mM), respectively. Below 1.50 mbsf at Site 16GH-P3, Cl^- concentration significantly increases and remains constant (~552 mM). Similarly, at Site 16GH-P4, Cl^- concentration gradually increases and maintains a constant value (~571 mM) from 1.28 mbsf to 4.55 mbsf. It reaches a maximum value (609 mM) at approximately 5.58 mbsf ~ 6.05 mbsf at Site 16GH-P4 (Figure 3A; Supplementary Table 1). In contrast, the second group, observed at Sites 16GH-P1 and 16GH-P5 (non-chimney sites), exhibits a constant Cl^- concentration (~533 mM) without significant variation with depth. The downcore profile of Na^+ concentrations at each site generally follows a trend similar to that of Cl^- (Figure 3A).

The SO_4^{2-} concentration at all sites decreases from the seawater value (~30 mM; UBGH2 Scientists, 2010) to ~0 mM (Figure 3A; Supplementary Table 1). The current SMT (hereafter SMT) depth is determined by extrapolating the depth where the SO_4^{2-} concentration reaches 0 mM. The estimated SMT depth of Sites 16GH-P3 and 16GH-P4 (chimney sites) is located at 1.9 mbsf and 2.5 mbsf, respectively, whereas it reaches 4.3 mbsf and 2.7 mbsf at Sites 16GH-P1 and 16GH-P5 (non-chimney sites), respectively. (Table 1). The maximum Ba^{2+} concentration in each site is observed around the SMT and Site 16GH-P3 has the lowest maximum Ba^{2+} concentration among the study sites (Figure 3A).

The alkalinity ranging from 8.9 mM to 60.8 mM increases from the seafloor to the SMT and then shows relatively constant concentration at Site 16GH-P3 or a slightly increasing trend at Sites 16GH-P1, 16GH-P4, and 16GH-P5 (Figure 3A; Supplementary Table 1). In contrast, the downcore profiles of Ca^{2+} and Sr^{2+} concentrations have decreasing trends at all sites. The Mg^{2+} concentration is constant at Sites 16GH-P1 and 16GH-P3 but shows an increasing trend with depth at Sites 16GH-P4 and 16GH-P5. At all sites, the K^+, H_4SiO_4, and B concentrations are generally higher than those in seawater (Figure 3A; Supplementary Table 1). The δD and $\delta^{18}O$ values in pore fluids at all sites vary in narrow ranges from -2.8‰ to 0.2‰ and from -0.2‰ to 0.3‰, respectively. The downcore profile of $\delta^{18}O$ at Site 16GH-P4 shows a slightly decreasing trend compared to other sites. The $\delta^{13}C_{DIC}$ value in pore fluid varies from -28.2‰ to 5.3‰.

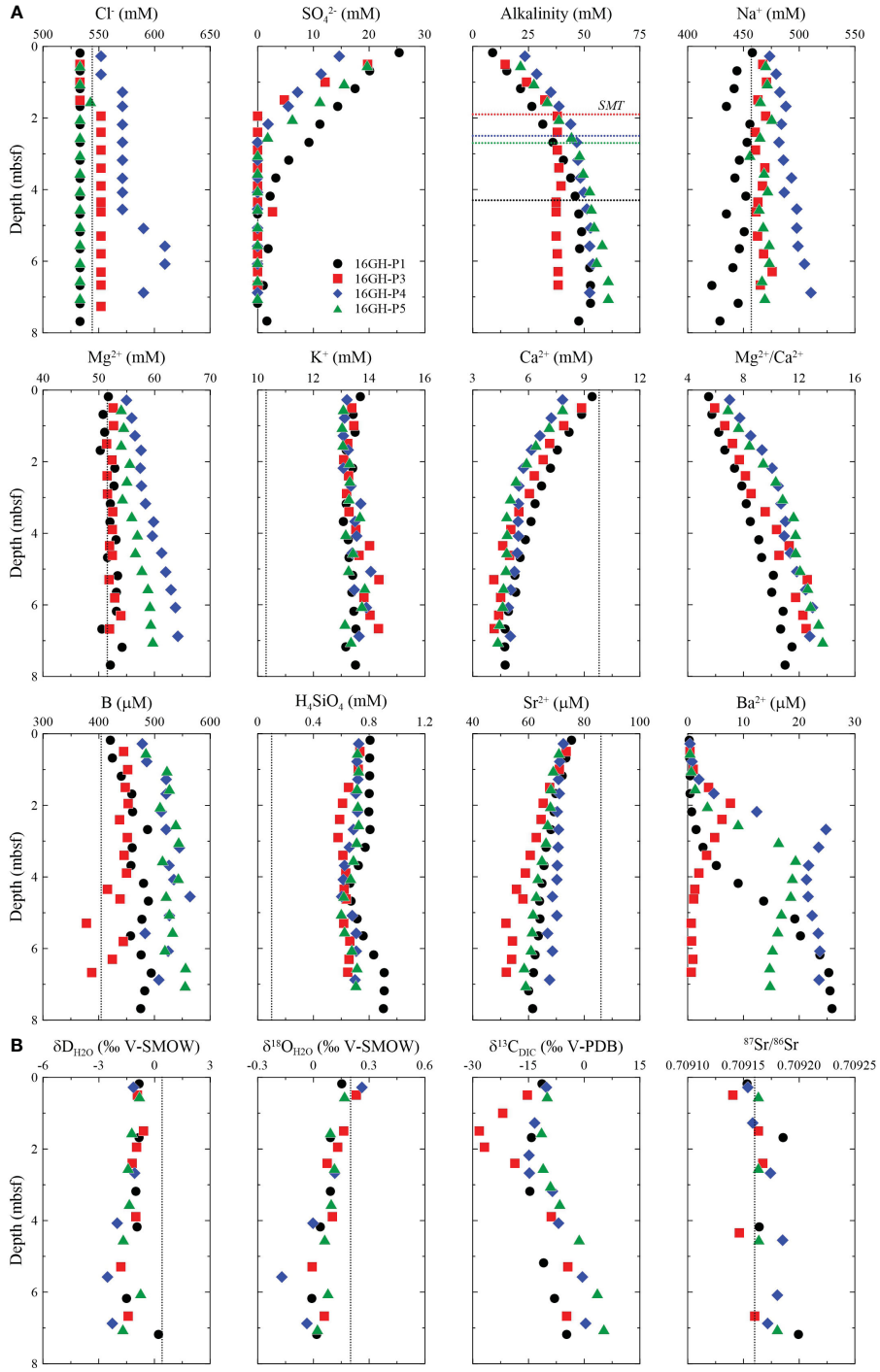

FIGURE 3
Downcore profiles of **(A)** Cl^-, SO_4^{2-}, alkalinity, Na^+, Mg^{2+}, K^+, Ca^{2+}, Mg^{2+}/Ca^{2+}, B, H_4SiO_4, Sr^{2+}, and Ba^{2+}, and **(B)** δD_{H2O}, $\delta^{18}O_{H2O}$, $\delta^{13}C_{DIC}$, and $^{87}Sr/^{86}Sr$ in pore fluids from Sites 16GH-P1, 16GH-P3, 16GH-P4, and 16GH-P5. The horizontal black, red, blue, and green lines in the downcore profile of alkalinity represent the current SMT depth at Sites 16GH-P1, 16GH-P3, 16GH-P4, and 16GH-P5, respectively. The vertical black dashed lines represent the chemical concentration and isotopic ratios of seawater from the Ulleung Basin (UBGH2 Scientists, 2010; Kim et al., 2013).

The minimum $\delta^{13}C_{DIC}$ value in each site is observed around the SMT, ~3.18 mbsf (-14.7‰) at Site 16GH-P1, ~1.50 mbsf (-28.2‰) at Site 16GH-P3, ~2.18 mbsf (-14.9‰) at Site 16GH-P4, and ~1.53 mbsf (-11.5‰) at Site 16GH-P5 (Figure 3B; Supplementary Table 1). The maximum $\delta^{13}C_{DIC}$ value is observed at 7.03 mbsf of Site 16GH-P5 (5.3‰). The $^{87}Sr/^{86}Sr$ ratios are relatively constant (0.70917 ± 0.00001, n = 19) (Figure 3B; Supplementary Table 1), which is similar to that of the open seawater (~0.70917; Paytan et al., 1993) and seawater from the Ulleung Basin (~0.70917; Kim et al., 2013).

4.3 Geochemical properties of headspace gas

The CH_4 is the primary hydrocarbon component in headspace gas samples at all sites, while C_{2+} is the trace composition. The CH_4 concentration is the lowest near the seafloor (< 300 ppm vol.) and increases sharply below the SMT (> 2,900 ppm vol.) (Figure 4A; Supplementary Table 2), irrespective of the seismic structures. The C_1/C_{2+} ratios at Sites 16GH-P3, 16GH-P4, and 16GH-P5 generally exceed 300, whereas they cannot be calculated at Site 16GH-P1 because the concentration of C_{2+} is below the detection limit. The CO_2 concentration does not show a distinct trend with depth, but its concentration varies from 1.0% vol. to 4.0% vol. at all sites (Figure 4A; Supplementary Table 2). As the measured CO_2 concentrations in headspace gas samples are at least 25 times higher than that in the atmosphere (~420 ppm vol., https://www.climate.gov/news-features/understanding-climate/climate-change-atmospheric-carbon-dioxide), the influence of atmospheric CO_2 in headspace gas is negligible.

The values of $\delta^{13}C_{CH4}$, δD_{CH4}, and $\delta^{13}C_{CO2}$ range from -85.9‰ to -67.2‰, from -204‰ to -190‰, and from -24.8‰ to -16.1‰, respectively. The minimum values for $\delta^{13}C_{CH4}$ and $\delta^{13}C_{CO2}$ generally occur near the SMT and increase with depth below the SMT (Figure 4B; Supplementary Table 2).

4.4 Petrography, mineralogy, isotopic compositions, and age of MDACs

MDACs can be roughly subdivided into three types based on their morphology: 1) massive-porous type, 2) massive-laminated type, and 3) semi-/un-consolidated type (Figure 2B). Massive-porous MDACs (a and c in Figure 2B) are mainly composed of microcrystalline magnesian calcite (Mg-calcite), fibrous aragonite, bioclasts, and detrital fragments (Figures 5B–D). Bioclasts, planktonic foraminifers, diatoms, and radiolarians are the dominant biogenic components of this type; framboidal pyrite is often found within the inner walls of shells. Massive-laminated MDACs (d in Figure 2B) have a massive and slightly wavy-laminated structure with a small number of bioclasts. The average thickness of the lamination varies from 1 mm to 2 mm, and planktonic foraminifers are randomly dispersed in the matrix (Figure 5A). Detrital fragments are also found as a form of anhedral and/or subhedral crystals (Figure 5E). Semi-/un-consolidated MDACs (b in Figure 2B) mainly consist of a microcrystalline matrix with many irregular-shaped pores. In the matrix, diatomaceous fragments with many shapes and sizes are found (Figure 5F).

The content of carbonate minerals in MDACs ranges from 25.6 wt.% of bulk MDAC to 87.8 wt.% of bulk MDAC (Supplementary

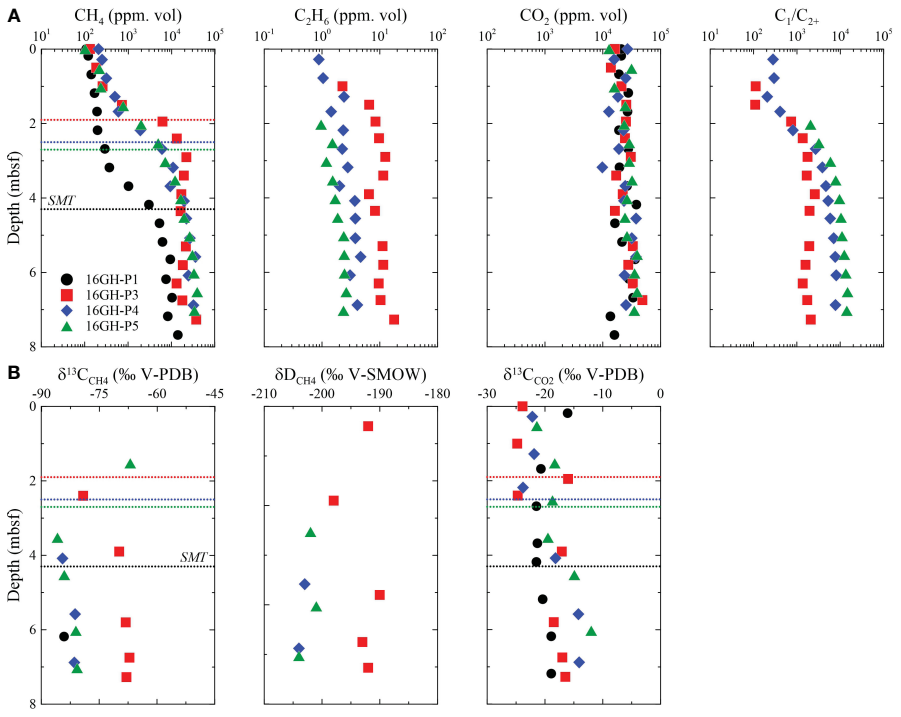

FIGURE 4
Downcore profiles of **(A)** CH_4, C_2H_6, CO_2, and C_1/C_{2+}, and **(B)** $\delta^{13}C_{CH4}$, δD_{CH4}, and $\delta^{13}C_{CO2}$ of headspace gas samples from Sites 16GH-P1, 16GH-P3, 16GH-P4, and 16GH-P5. The dashed line represents the current SMT in each site (black: Site 16GH-P1, red: Site 16GH-P3, blue:16GH-P4, green: Site 16GH-P5).

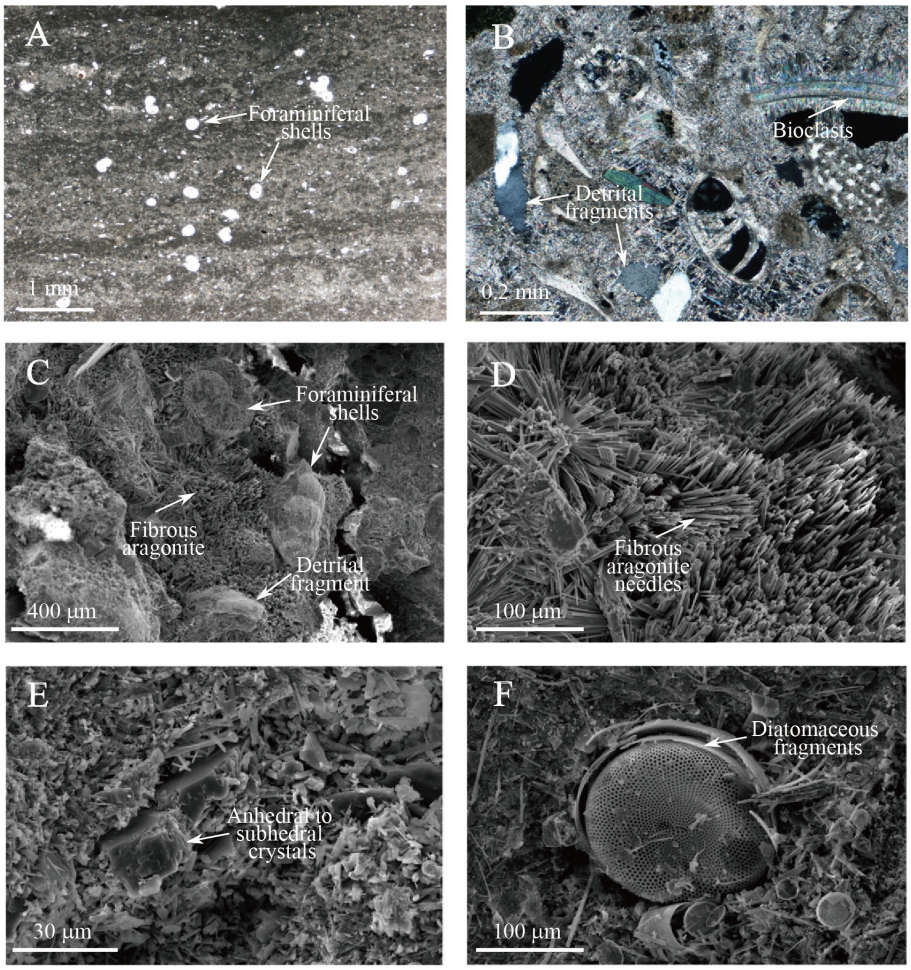

FIGURE 5
Photomicrographs and scanning electron micrographs of MDACs. **(A)** Authigenic carbonate of the massive-laminate type from 6.90 mbsf at Site 16GH-P4. White spots indicate planktonic foraminiferal shells. **(B)** Bioclasts are abundant, and aragonite is present as acicular cement and microcrystalline matrix from 1.48 mbsf at Site 16GH-P3. **(C-D)** Bioclasts and detrital fragments are cemented by fibrous aragonite crystals from 1.48 mbsf of Site 16GH-P3. **(E)** Matrix of microcrystalline magnesian calcite with anhedral and/or subhedral crystals with a few µm in size at 6.90 mbsf of Site 16GH-P4. **(F)** Diatomaceous fragments are found in many shapes and sizes at 7.69 mbsf of Site 16GH-P3.

Table 3). Calcite, aragonite, and Mg-calcite are the dominant carbonate minerals of MDACs, and dolomite is minor (< 1 wt.% of bulk MDAC). MDACs from 7.69 mbsf at Site 16GH-P3 and from 6.63 mbsf, 6.90 mbsf, and 7.33 mbsf at Site 16GH-P4 have a high aragonite content (> 49.5 wt.% of bulk MDAC), whereas MDACs from 3.30 mbsf at Site 16GH-P3 and 5.70 mbsf at Site 16GH-P4 contain abundant Mg-calcite (> 50 wt.% of bulk MDAC). The non-carbonate minerals in MDACs mainly consist of silicates (plagioclase, K-feldspar, quartz, illite, and chlorite) as detrital components (Figure 6A; Supplementary Table 3).

The $\delta^{13}C_{MDAC}$ and $\delta^{18}O_{MDAC}$ values vary from -43.0‰ to -31.3‰ and from 3.9‰ to 5.8‰ at Site 16GH-P3, and from -44.9‰ to -41.7‰ and from 4.1‰ to 5.7‰ at Site 16GH-P4, respectively. MDACs above a depth of 1.50 mbsf at Site 16GH-P3 exhibit higher $\delta^{13}C$ (> -34.3‰) and lower $\delta^{18}O$ (< 4.1‰) values compared to those found below this depth ($\delta^{13}C$ = -43.1‰ ~ -41.6‰; $\delta^{18}O$ = 5.5‰ ~ 5.8‰) (Figure 6B; Supplementary Table 3). Except for these two MDACs, the $\delta^{13}C_{MDAC}$ values are constant (-44.9‰ ~ -41.6‰) at Sites 16GH-P3 and 16GH-P4, irrespective of the morphology. In contrast, the $\delta^{18}O_{MDAC}$ value is the lowest (4.1‰) in the massive-laminated MDAC from Site 16GH-P4 (Supplementary Table 3).

U-Th ages of MDACs are presented in Figure 2A and Supplementary Table 3, although they have large errors. The corrected U-Th ages of the MDAC at 1.48 mbsf of Site 16GH-P3 range from 29.3 ± 15.7 ka BP to 38.5 ± 12.4 ka BP (n = 3). The age at 6.90 mbsf and 7.33 mbsf of Site 16GH-P4 varies from 20.3 ± 8.0 ka BP to 23.5 ± 12.2 ka BP (n = 3) and from 23.4 ± 4.3 ka BP to 24.1± 4.7 ka BP (n = 2), respectively (Figure 2A; Supplementary Table 3). The MDAC from Site 16GH-P3 has an older age than those from Site 16GH-P4.

5 Discussion

5.1 Sedimentary facies distribution and depositional environment

The BM facies was mainly observed from the seafloor to 5.90 mbsf and 6.39 mbsf at Sites 16GH-P1 and 16GH-P5 (non-chimney

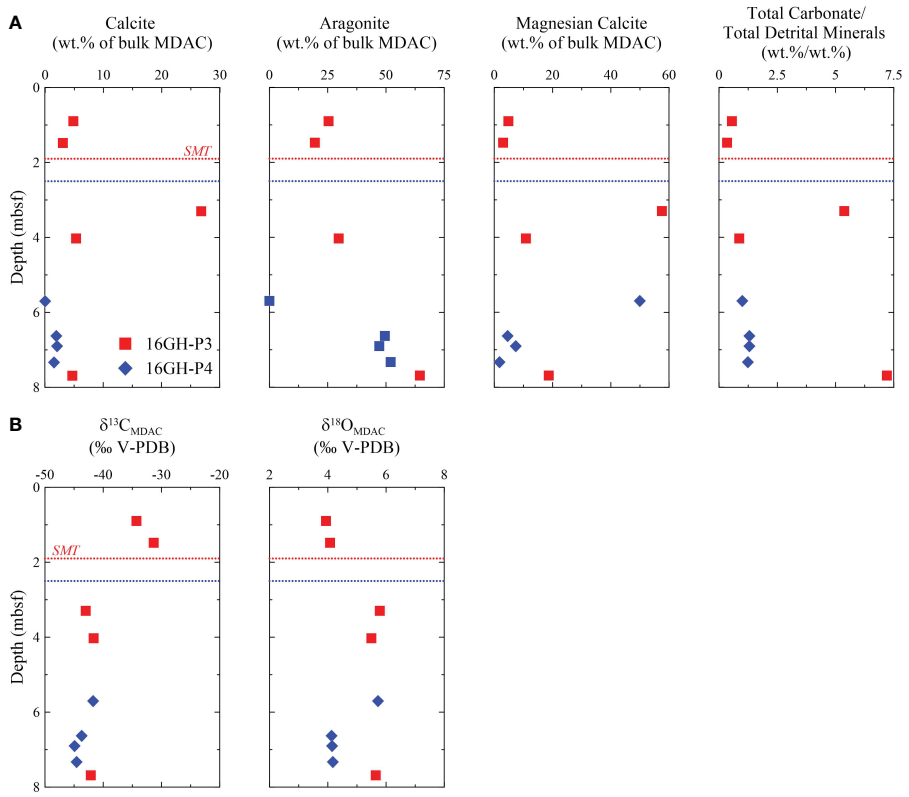

FIGURE 6
Downcore profiles of **(A)** calcite, aragonite, and magnesian calcite content, and total carbonate/total detrital minerals by XRD analysis, and **(B)** $\delta^{13}C$ and $\delta^{18}O$ in MDACs from Sites 16GH-P3 and 16GH-P4. The horizontal red and blue dashed lines represent the current SMT depth at Sites 16GH-P3 and 16GH-P4, respectively.

sites), respectively, while the relatively thin SLM, BSM, and HM appeared below these depths (Figure 2A). The BM interval represents hemipelagic sediment deposition under well-oxygenated conditions (Tada et al., 1999; Gorbarenko and Southon, 2000) during the high sea-level period of marine isotope stage (MIS) 1 (Park et al., 2006; KIGAM, 2016). In the lower part of 16GH-P1, the BM facies changes into BSM facies (Figure 2A). This facies was formed by the increase in coarser sediments, such as sandy particles, which were probably derived from the neighboring continental shelf during the sea invasion period after the Last Glacial Maximum (KIGAM, 2016). The period of sedimentary deposition at Sites 16GH-P1 and 16GH-P5 was estimated to cover the early post-glacial of Late Pleistocene to Holocene high sea-level period.

Sites 16GH-P3 and 16GH-P4 (chimney sites) contain abundant MDACs as randomly scattered nodules or layers form (ACM and ACL facies in Figure 2A). In particular, this distribution pattern of MDACs is well developed in the sediments throughout the core at Site 16GH-P3. At Site 16GH-P4, the LM and SLM facies are thick at the top of the core (0.1 mbsf to ~5.4 mbsf). According to the previous studies (e.g., KIGAM, 2016), it was interpreted that the GH chimney mound underwent a sequential process involving formation, uplift to the sea floor, and erosion. Subsequently, LM and SLM facies at Site 16GHP-P4 were formed during the deglacial phase at the top of the core. The U-Th dating of MDACs also indicates that the top interval of ~5.4 mbsf at Site 16GH-P4 was deposited during a younger period than that of Site 16GH-P3 (Figure 2A).

The matrix of porous MDACs primarily comprises microcrystalline Mg-calcite, and their cavities are mostly filled with aragonite in the form of acicular needles or sometimes botryoidal cement. Fibrous cements and micritic laminated fabrics are also observed in this type of MDAC (Figure 5; Supplementary Table 3). These observations provide evidence for the mixing of methane-rich fluids with seawater and/or the presence of methane and sulfide (e.g., Peckmann et al., 2001; Magalhães et al., 2012).

5.2 Source of pore fluid and CH_4 gas

Cl^- concentrations and isotopic values of water (δD and $\delta^{18}O$) in pore fluids at Sites 16GH-P1 and 16GH-P5 vary in narrow ranges throughout the entire cores (Cl^- = 533 mM ~ 543 mM, δD = -1.7‰ ~ 0.2‰, $\delta^{18}O$ = 0.0‰ ~ 0.2‰) (Figures 3, 7; Supplementary Table 1), and are close to the values of the present-day bottom seawater (Cl^- = 544 mM, $\delta^{18}O$ = 0.2‰, δD = 0.4‰) from the Ulleung Basin (UBGH2 Scientists, 2010; Kim et al., 2013). Hence, the source of pore fluids at these sites mainly originates from ambient seawater. At Site 16GH-P4, Cl^- concentrations are higher

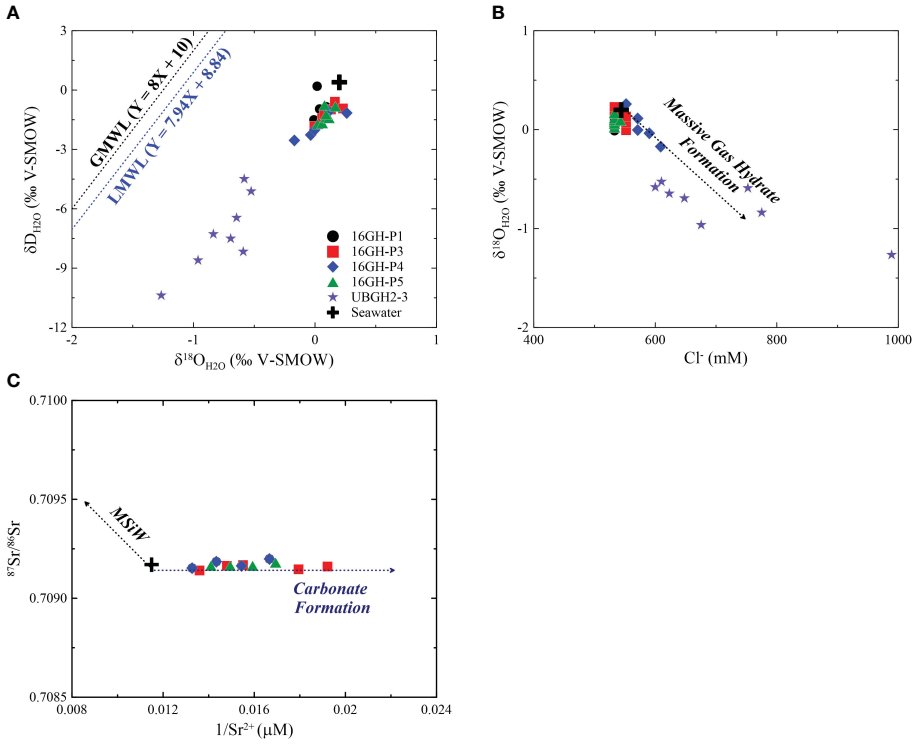

FIGURE 7
Scatter plots of **(A)** δD_{H2O} versus $\delta^{18}O_{H2O}$, **(B)** $\delta^{18}O_{H2O}$ versus Cl^-, and **(C)** $^{87}Sr/^{86}Sr$ versus $1/Sr^{2+}$ in bottom seawater from Site UBGH2-3 and pore fluids from Sites 16GH-P1, 16GH-P3, 16GH-P4, 16GH-P5, and UBGH2-3 (UBGH2 Scientists, 2010; Kim et al., 2013). The δD and $\delta^{18}O$ data of seawater and pore fluid from Site UBGH2-3 are from Kim et al. (2013). The GMWL is the global meteoric water line (Craig, 1961) and the LMWL is the local meteoric water line (Lee et al., 1999). The trend of massive gas hydrate formation in Figure 7B is modified from Tomaru et al. (2006) and the trends of carbonate formation and MSiW in Figure 7C are adapted from Kim et al. (2016). MSiW is marine silicate weathering.

than that of seawater and vary from 591 mM to 609 mM below 5.08 mbsf (Figure 3A; Supplementary Table 1). However, the water stable isotopes (δD and $\delta^{18}O$) at this site generally have lower values (δD = -2.5‰ ~ -1.1‰, $\delta^{18}O$ = -0.2‰ ~ 0.3‰) than those at the other studied sites (δD = -1.8‰ ~ 0.2‰, $\delta^{18}O$ = 0.0‰ ~ 0.2‰), and there is a linear correlation between them (r^2 = 0.85) (Figure 7A; Supplementary Table 1). Furthermore, $\delta^{18}O$ and Cl^- exhibit a negative correlation (r^2 = 0.72) (Figure 7B). During the MIS 2 in the Ulleung Basin, seawater had a low $\delta^{18}O$ value by the freshening of surface water associated with the isolation from the Pacific Ocean (Kim et al., 2000; Lee, 2007; Wu et al., 2020), which is a plausible source for the low $\delta^{18}O$ values of pore fluids. However, this fluid cannot account for the observed high Cl^- concentration in pore fluid at this site. Such characteristics have usually been reported in the bottom water and/or pore fluid in Arctic regions (Alexeev and Alexeeva, 2003; Charkin et al., 2017; Kim et al., 2022) as a result of the formation of submarine ice and/or permafrost within the sediments. Since the water and sediment columns in the southern Ulleung Basin have not been frozen annually, these mechanisms are not attributed to high Cl^- concentration with low δD and $\delta^{18}O$ values in pore fluid observed at Site 16GH-P4. Instead, this can be attributed to the formation of massive GH near the seafloor within fine-grained sediment layers, such as mud, characterized by low permeability (Torres et al., 2004; Riedel et al., 2006; Tomaru et al., 2006; Collett et al., 2008; Hong et al., 2017). In general, when massive GHs form near the seafloor sediment in this layer associated with high upward gas flux, pore fluids exhibit higher Cl^- concentrations and lower δD and $\delta^{18}O$ values in comparison to fluids from the non-GH bearing intervals. Conversely, heavy water isotopes (δD and $\delta^{18}O$) tend to be preferentially incorporated into the clathrate structure. These occur because the fluid released during GH formation does not equilibrate with the pore fluid in the surrounding sediment layers due to low permeability. In contrast, during the formation of the disseminated GH in the sand layer, the pore fluids in the GH-bearing intervals equilibrate with the surrounding sediment fluids due to their high permeability. Consequently, this leads to similar Cl^- concentrations as well as δD and $\delta^{18}O$ values in pore fluids from both GH-bearing and non-GH bearing intervals. Although massive and/or disseminated GHs were not found in the cores investigated, Site 16GH-P4 is located ~0.1 km from Site UBGH2-3, where high Cl^- concentrations (maximum Cl^- = ~1440 mM) and low δD and $\delta^{18}O$ values (minimum δD = ~-14.7‰; minimum $\delta^{18}O$ = ~-1.6‰) have been reported in fluids collected from massive GHs-bearing intervals below 6 mbsf during the UBGH2 Expedition (Kim et al., 2013; Hong et al., 2014). Hence, it is postulated that the similar trends in Cl^- concentrations and δD and $\delta^{18}O$ values in pore fluids at Site 16GH-P4 are impacted by massive GH formation occurring below the depth of retrieved core.

The Cl^- concentrations below 1.95 mbsf (~552 mM) at Site 16GH-P3 are slightly higher than those above this depth (~533

mM), and there is no significant change in δD and $\delta^{18}O$ values throughout the entire sampling depth (Figures 3, 7; Supplementary Table 1). The pore fluid would be potentially influenced by the water-rock interactions or the fluids migrated from the deep sediment; however, the exact mechanism cannot be identified given the dataset.

High C_1/C_{2+} ratios (commonly > 300) in headspace gas samples from Sites 16GH-P1, 16GH-P3, 16GH-P4, and 16GH-P5 (Figures 4A, 8; Supplementary Table 2) indicate that CH_4 predominantly originates from microbial source rather than thermogenic source (Bernard et al., 1978; Whiticar, 1999; Pape et al., 2010; Kim et al., 2011; Kim et al., 2012; Choi et al., 2013; Milkov and Etiope, 2018). The $\delta^{13}C_{CH4}$, δD_{CH4}, and $\delta^{13}C_{CO2}$ values consistently support this interpretation. All headspace gas samples plotted in the region of microbial CH_4 origin via the CO_2 reduction in the diagram, displaying the relationship between $\delta^{13}C_{CH4}$ and C_1/C_{2+} (Figure 8A; Supplementary Table 2). Furthermore, the diagrams depicting the relationships of $\delta^{13}C_{CH4}$ versus δD_{CH4} and $\delta^{13}C_{CH4}$ versus $\delta^{13}C_{CO2}$ provide additional evidence for the microbial CH_4 origin via the CO_2 reduction pathway (Figures 8B, C). This observation aligns with the outcomes of numerous prior investigations conducted in the Ulleung Basin (Kim et al., 2011; Kim et al., 2012; Choi et al., 2013; Kim et al., 2013).

5.3 Occurrence of ongoing marine silicate weathering (MSiW)

Alkalinity in pore fluids above and within the SMT is usually produced by organic matter degradation via POCSR and AOM that consumes SO_4^{2-} as the main electron acceptor. Assuming SO_4^{2-} is mainly derived from the overlying seawater for these reactions (~30 mM; UBGH2 Scientists, 2010), alkalinity can be maximized up to ~60 mM by POCSR and ~30 mM by AOM with the complete consumption of SO_4^{2-}. Hong et al. (2014) have revealed that AOM is a dominant reaction for both carbon and sulfur cycles around the SMT, accounting for at least 85% of these cycles within the chimney structures of the Ulleung Basin in comparison with POCSR. As Sites 16GH-P3 and 16GH-P4 show chimney structures in the subsurface (Figure 1; see Section 2 "Regional Setting"), we can estimate the maximum alkalinity around the SMT of these sites as < ~35 mM by the simple mixing model of two end-members given that the POCSR:AOM is 0.15:0.85. The alkalinity should be lower than this value because of the ongoing carbonate precipitation within the sediment column at both sites as inferred from the decreasing downcore profile of Ca^{2+} and Sr^{2+} concentrations in pore fluids and the existence of MDACs (Figures 2, 3A). However, the measured alkalinity concentrations in the pore fluid around the SMT of Sites

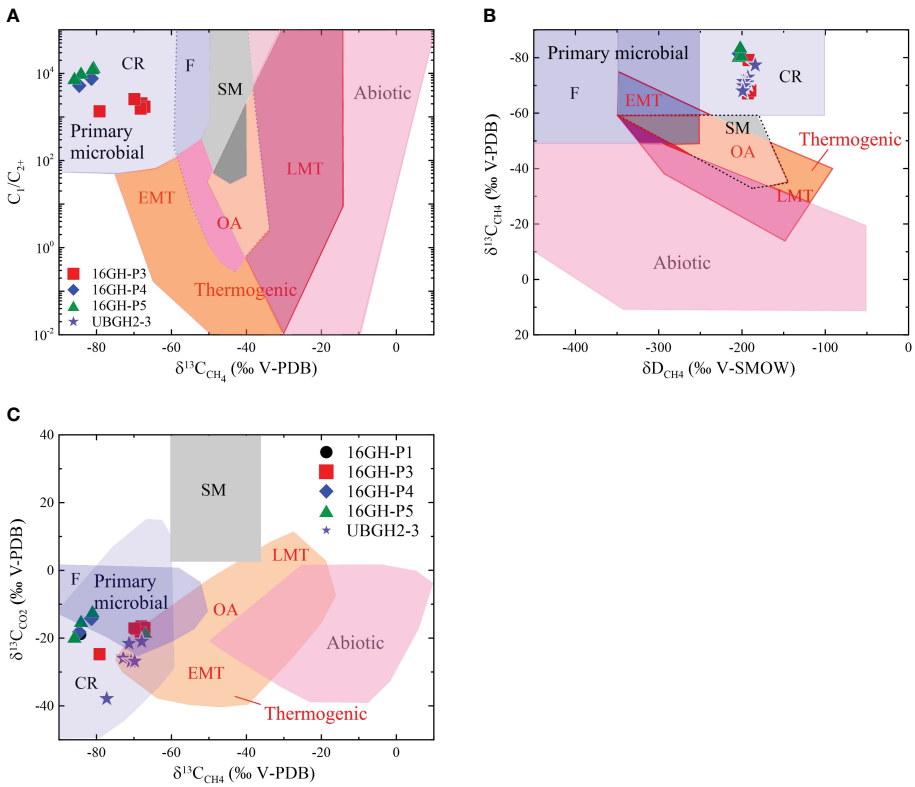

FIGURE 8
(A) Genetic diagram of C_1/C_{2+} versus $\delta^{13}C_{CH4}$ (after Milkov and Etiope, 2018) of headspace gas samples from Sites 16GH-P3, 16GH-P4, 16GH-P5, and UBGH2-3. **(B)** $\delta^{13}C_{CH4}$ versus δD_{CH4} diagram of headspace gas samples from Sites 16GH-P3, 16GH-P4, 16GH-P5, and UBGH2-3 (after Milkov and Etiope, 2018). **(C)** Genetic diagram of $\delta^{13}C_{CH4}$ versus $\delta^{13}C_{CO2}$ (after Milkov and Etiope, 2018) of headspace gas samples from Sites 16GH-P1, 16GH-P3, 16GH-P4, 16GH-P5, and UBGH2-3. The gas compositions and isotopic values of headspace gas samples are from Site UBGH2-3 (KIGAM, 2011). CR, CO_2 reduction; F, methyl-type fermentation; SM, secondary microbial; EMT, early mature thermogenic gas; OA, oil-associated thermogenic gas; LMT, late mature thermogenic gas.

16GH-P3 and 16GH-P4 are ~38 mM and ~45 mM (Figure 3A; Supplementary Table 1), respectively, which (slightly) exceed the estimated concentration. In addition, the downcore alkalinity profile has an increasing trend below the SMT at Sites 16GH-P1, 16GH-P4, and 16GH-P5 (Figure 3A; Supplementary Table 1). These trends are not common and suggest that additional reactions should occur to account for the excess alkalinity in the fluid. The dissolved K^+, B, and H_4SiO_4 in most pore fluid samples from all sites show higher concentrations than those of bottom seawater (K^+ = 10.3 mM, B = 404 μM, H_4SiO_4 = 0.4 mM) (UBGH2 Scientists, 2010; Kim et al., 2013) as alkalinity increases. Additionally, the Mg^{2+} concentration of fluids from Sites 16GH-P4 and 16GH-P5, which mostly range from 54 mM to 64 mM, displays higher concentration than the bottom seawater (~51 mM; UBGH2 Scientists, 2010; Kim et al., 2013), with an increasing downcore profile (Figure 3A; Supplementary Table 1). Kim et al. (2016) have shown a similar result from the pore fluid at Site UBGH2-1_1 (Figure 1A) collected during the UBGH2 Expedition and this result was attributed to marine silicate weathering (MSiW) that converts CO_2 into alkalinity and releases dissolved cations in an anoxic marine system. Our fluid data also point to the occurrence of MSiW in the Ulleung Basin, which significantly impacts the geochemical properties of the pore fluids.

5.4 Influence of CH_4 and seawater on MDAC precipitation

The decreasing downcore profile of Ca^{2+} and Sr^{2+} concentrations at all cores investigated in this study generally shows a similar trend to that of SO_4^{2-} (Figure 3A). These results indicate that continuous carbonate precipitation takes place within the sediments, leading to the consumption of Ca^{2+} and Sr^{2+} in pore fluids (see Equation 3). The relationship between $^{87}Sr/^{86}Sr$ and $1/Sr^{2+}$ (Figure 7C) also supports this interpretation (Kim et al., 2016). Indeed, massive authigenic carbonates were found at Sites 16GH-P3 and 16GH-P4 (Figure 2). The measured $\delta^{13}C_{MDAC}$ values (-44.9‰ to -31.3‰) (Figure 6B; Supplementary Table 3) are lower than those of the organic matter reported in the Ulleung Basin (-24‰ to -21‰) (Choi et al., 2013; Kim et al., 2014) and the measured minimum $\delta^{13}C_{DIC}$ (-28.3‰ and -14.7‰ at Sites 16GH-P3 and 16GH-P4, respectively) in pore fluids (Figure 3; Supplementary Table 1). Hence, the $\delta^{13}C_{MDAC}$ value indicates the presence of an additional DIC source with a lower carbon isotopic value compared to that of pore fluids and organic matter within this basin when MDAC forms. We postulate that the migrating upward fluid, which contains ^{13}C-depleted CH_4 from the deep-seated sediment, is a reasonable source, as this fluid is involved in AOM around the SMT. This process leads to an increase in alkalinity via the production of bicarbonate (HCO_3^-) and subsequent MDAC precipitation (Paull et al., 1992; Aloisi et al., 2000; Peckmann et al., 2001; Aloisi et al., 2002; Naehr et al., 2007; Pierre et al., 2014; Crémière et al., 2016). Consequently, the carbon isotopic property of CH_4 migrating upward significantly inherits that of MDACs produced around the SMT. In general, the $\delta^{13}C_{MDAC}$ values associated with thermogenic CH_4 typically range from ~-40‰ to -20‰, while the values are less than -40‰ via AOM using microbial CH_4 (Naehr et al., 2007; Crémière et al., 2016; Crémière et al., 2018). $\delta^{13}C_{MDAC}$ values of all MDACs from Site 16GH-P4 that show massive-porous and -laminated morphologies are < -41.7‰ (Figure 6B; Supplementary Table 3), thus, AOM that mainly uses microbial CH_4 is incorporated to form MDACs. This finding is consistent with the CH_4 source in headspace gas samples near and below the SMT at this site (-88.0‰ < $\delta^{13}C_{CH4}$ < -81.5‰) (Figure 4; Supplementary Table 2). On the other hand, the wide range of $\delta^{13}C_{MDAC}$ values at Site 16GH-P3 implies that gas sources involved in the MDAC formation rely on the sampling depth (Figure 6B; Supplementary Table 3); 1) massive-porous MDACs above the SMT are related to thermogenic CH_4 ($\delta^{13}C_{MDAC}$ > -35.0‰), and 2) MDACs with semi-consolidated and massive-porous and -laminated morphologies below the SMT are associated with microbial CH_4 ($\delta^{13}C_{MDAC}$ = ~-42‰). $\delta^{13}C_{CH4}$ values (< -67.2‰) in all headspace gas samples below the SMT from Site 16GH-P3 (Figure 4; Supplementary Table 2) indicate that CH_4 has a predominantly microbial origin. In addition, to date, studies have revealed that the CH_4 from the seafloor to 250 mbsf in the Ulleung Basin is microbial origin via CO_2 reduction (Figure 8) based on geochemical features of headspace gas samples from the UBGH2 Expedition as well as other expeditions (Kim et al., 2012; Choi et al., 2013). Hence, thermogenic CH_4 does not involve AOM reaction and MDAC formation in the Ulleung Basin. Rather, the ^{13}C-enriched MDACs are likely affected by HCO_3^- from ambient seawater at this site because these MDACs have often been found in the sediment above the SMT (Peckmann and Thiel, 2004; Crémière et al., 2016; Pierre et al., 2017). The XRD results of MDACs, which display that aragonite and Mg-calcite are the predominant mineral compositions (Figure 6A; Supplementary Table 3), also support our interpretation. Theoretically, aragonite precipitation is kinetically favored in seawater-ventilated environments with high SO_4^{2-} concentration and it has generally low Mg^{2+}/Ca^{2+} ratios compared to high-Mg calcite (Burton, 1993; Mazzini et al., 2006). Indeed, MDACs are found at shallow sediment depth (< 8 mbsf) (Figure 2; Supplementary Table 3) where ambient seawater can influence sediments, and the Mg^{2+}/Ca^{2+} (5.9 to 12.8) in all pore fluids from Sites 16GH-P3 and 16GH-P4 have higher ratios compared to that of seawater (5.5) (Figure 3A; Supplementary Table 1). Thus, these results imply that sufficient conditions for the precipitation of aragonite and low-Mg calcite are provided at both Sites 16GH-P3 and 16GH-P4 rather than high-Mg calcite. Although MDAC morphology is not well matched with $\delta^{13}C_{MDAC}$, microscopic observations have revealed that massive-porous MDACs above the SMT contain abundant bioclasts, planktonic foraminifers, diatoms, radiolarians, and detrital fragments, as compared to MDACs below the SMT at Site 16GH-P3 (Figure 5B). The cavities in this type of MDAC (a and c in Figure 2B) can also act as conduit for CH_4-rich fluid and/or seawater migration due to their high porosity and permeability. Overall, the chemical properties of microbial CH_4 migrating upward are significantly inherited by MDACs at both Sites 16GH-P3 and 16GH-P4 whereas the properties of seawater prominently imprint MDACs found above the SMT at Site 16GH-P3.

5.5 Fluid source of MDAC

Carbonate minerals in MDACs from Sites 16GH-P3 and 16GH-P4 primarily consist of calcite, aragonite, and Mg-calcite, with minor amounts of dolomite. The proportions of calcite, aragonite, and Mg-calcite in the total carbonate minerals (sum of calcite, aragonite, dolomite, and Mg-calcite contents) at both sites range from 0% to 32%, from 3% to 100%, and from 0% to 94%, respectively (Supplementary Table 3). In general, the $\delta^{18}O_{MDAC}$ values are useful to reveal the fluid source during carbonate precipitation (e.g., Greinert et al., 2001; Naehr et al., 2007). Given that the $\delta^{18}O$ values of aragonite and calcite precipitated at isotopic equilibrium with temperature and $\delta^{18}O$ value of the bottom seawater in the Ulleung Basin, the theoretical $\delta^{18}O_{aragonite}$ and $\delta^{18}O_{calcite}$ values can be calculated using Equations 4 and 5, respectively (Kim and O'Neil, 1997; Kim et al., 2007).

$$\mathbf{1000ln\alpha_{aragonite-seawater}} = \mathbf{17.88} \times \frac{\mathbf{10^3}}{\mathbf{T}}\mathbf{(Kelvin)} - \mathbf{31.14} \quad (4)$$

$$\mathbf{1000ln\alpha_{calcite-seawater}} = \mathbf{18.03} \times \frac{\mathbf{10^3}}{\mathbf{T}}\mathbf{(Kelvin)} - \mathbf{32.42} \quad (5)$$

Assuming that the temperature and $\delta^{18}O$ value of the bottom seawater from Ulleung Basin at the present time are 0.5°C and 0.2‰ (V-SMOW) (UBGH2 Scientists, 2010; Kim et al., 2013), respectively, the theoretical $\delta^{18}O$ values of aragonite and calcite calculated by Equations 4 and 5 would be ~4.0‰ (V-PDB) and ~3.3‰ (V-PDB), respectively. The measured $\delta^{18}O_{MDAC}$ values above the SMT at Site 16GH-P3 are similar to the calculated $\delta^{18}O_{MDAC}$ value of aragonite (Supplementary Table 3), suggesting that pore fluid with a similar $\delta^{18}O$ value to that of present-day bottom seawater was involved during MDAC precipitation. For Site 16GH-P3, it is likely that the enrichment in ^{13}C for MDACs from above the SMT (> -34.3‰) compared to those from below the SMT (< -40%) is caused by incorporation of ^{13}C-rich HCO_3^- (~0‰) from seawater during carbonate precipitation (see Section 5.4). In contrast, the $\delta^{18}O_{MDAC}$ values (> ~5.5‰) below the SMT at Site 16GH-P3 and at 5.70 mbsf of Site 16GH-P4 are significantly higher than the calculated theoretical $\delta^{18}O$ values of both aragonite and calcite, implying that MDAC precipitation occurs in association with pore fluid characterized by higher $\delta^{18}O$ value and/or in marine environments with lower temperatures compared to the present seawater conditions. In order to align with the analyzed $\delta^{18}O_{MDAC}$ value (> ~5.5‰) calculated using Equation 5, the temperature has to be lower than -6°C. However, such temperatures are not reasonable, as they would result in the freezing of seawater and sediment. Therefore, we exclude the possibility of lower temperatures for the high $\delta^{18}O_{MDAC}$ values observed in the MDACs. A plausible explanation for these observed $\delta^{18}O_{MDAC}$ values is a fluid source with a high $\delta^{18}O$value. The typical characteristics of clay dehydration and opal diagenesis, such as relatively high $\delta^{18}O$ values with low Cl^- concentrations and relatively low $^{87}Sr/^{86}Sr$ values in pore fluid (Kastner et al., 1991; Kim et al., 2013; Kim et al., 2021; Kim et al., 2022), are not exhibited in fluids from Site 16GH-P3 (Figures 3, 7; Supplementary Table 1). Therefore, we rule out both reactions as sources for the fluid with a high $\delta^{18}O$ value that forms MDACs. Instead, it is reasonable that the fluid source for the formation of ^{18}O-rich MDACs shown below the SMT at Site 16GH-P3 and at 5.70 mbsf of Site 16GH-P4 is derived from GH dissociation. This interpretation is supported by the presence of numerous shallow GHs found in the Ulleung Basin (Kim et al., 2011; Kim et al., 2012; Choi et al., 2013; Kim et al., 2013).

MDACs were collected from 5.70 mbsf to 7.33 mbsf at Site 16GH-P4 (Figure 2; Supplementary Table 3) thus, we anticipated that $\delta^{18}O$ values of MDACs are similar at all sampling intervals within this site. However, these values below 6.63 mbsf are significantly lower than that of 5.70 mbsf at Site 16GH-P4 (up to ~1.5‰), but slightly higher than those above 1.48 mbsf at Site 16GH-P3 (Figure 6B; Supplementary Table 3). The findings suggest that the fluid source contributing to MDACs precipitation underwent significant changes within a 2 m interval of the sediment column (Figure 6B, Supplementary Table 3). The MDAC from 5.70 mbsf appears to inherit its properties from the fluid with a higher $\delta^{18}O$ value, while the other MDACs have primarily originated from fluid with $\delta^{18}O$ values similar to that of the present ambient seawater. However, this interpretation of the rapid change in the fluid source for MDACs is not reasonable in the natural marine system. Thus, this observation remains unexplained.

Kim et al. (2013) revealed that pore fluids with high Cl^- concentration at Site UBGH2-3 have relatively low $\delta^{18}O$ values (< -0.5‰) due to the formation of massive GHs (Figure 7B). In addition, pore fluid from Site 16GH-P4 is characterized by increasing Cl^- concentration and decreasing $\delta^{18}O$ value as fluid sampling depth increases, in comparison to other sites (Figure 3B). It is postulated that massive GHs were probably present below the sampling depth of the retrieved core at Site 16GH-P4 and may have influenced the isotopic composition of the pore fluid, as indicated by the observed low $\delta^{18}O$ value (-0.5‰) at this site. This fluid may contribute to the precipitation of MDACs under the same temperature conditions as the bottom seawater. Under these circumstances, the theoretical $\delta^{18}O$ values of aragonite and calcite calculated by Equations 4 and 5 are ~3.3‰ (V-PDB) and ~2.6‰ (V-PDB), respectively. These values are lower than the measured $\delta^{18}O_{MDAC}$ below 6.63 mbsf at Site 16GH-P4 (Figure 6; Supplementary Table 3). In comparison to the $\delta^{18}O_{MDAC}$ value above 6.63 mbsf at Site 16GH-P4, we postulated that the lower $^{18}O_{MDAC}$ values in this interval can be attributed to residual fluid derived from the massive GH formation.

5.6 Significance of MSiW and MDAC precipitation

Both MSiW and carbonate precipitation play an important role in carbon sinks in the global carbon cycle. Large amounts of dissolved cations and alkalinity released into fluids by MSiW are involved in authigenic carbonate formation (Wallmann et al., 2008; Scholz et al., 2013; Solomon et al., 2014; Torres et al., 2020). Recently, the rate of carbon fixation by carbonate precipitation associated with MSiW has been estimated to be on the order of 10^{12}

mole C yr^{-1} (Torres et al., 2020). It has also been revealed that the maximum alkalinity of pore fluid on the Krishna-Godavari Basin, Indian Margin, in association with ongoing MSiW is less than 45 mM (Solomon et al., 2014) because authigenic carbonate formation consumes the excess alkalinity released by this reaction. Indeed, many MDACs have been documented at this margin (e.g., Teichert et al., 2014). Therefore, both MSiW and MDAC significantly impact on pore fluid geochemistry in the Krishna-Godavari Basin and the Ulleung Basin.

Many MDACs were found at Sites 16GH-P3 and 16GH-P4 (Figure 2; Supplementary Table 3). Compared to the Krishna-Godavari Basin, the maximum alkalinity in pore fluids sampled from the MDAC-bearing interval has a similar concentration at Site 16GH-P3 (< 40 mM), whereas it has a higher concentration at Site 16GH-P4 (up to 54 mM). Additionally, this concentration at Site 16GH-P4 is similar to or slightly lower than those at non-MDAC-bearing sites (Sites 16GH-P1 and 16GH-P5) in this study and many previous investigations in the basin (e.g., UBGH2-1_1; Kim et al., 2013; Kim et al., 2016). Considering that the ACM and ACL facies were observed throughout the retrieved core length of Site 16GH-P3 whereas they were exclusively found below 5.4 mbsf at Site 16GH-P4. MDAC precipitation is likely to be more pronounced at the former site. Pore fluid chemistry in the southern Ulleung Basin from this study also clearly points out the occurrence of MSiW. Since Kim et al. (2016) have documented that the MSiW occurs without MDAC observations in the Ulleung Basin, MDAC and pore chemistry results from this study provide the first evidence for the ongoing occurrence of both reactions in the basin. Moreover, the higher alkalinity (> 45 mM) at Site 16GH-P4 implies that the alkalinity produced by MSiW is much greater in the Ulleung Basin than in the Indian Margin, although it is masked by authigenic carbonate precipitation as a carbon sink. The high alkalinity in pore fluid from the Ulleung Basin is a unique characteristic and plays an important role in the linkage with the carbon cycle in this basin. The cations released by MSiW, such as dissolved Ca^{2+}, Mg^{2+}, B, and H_4SiO_4, also play a pivotal role in impacting the diagenesis and element cycles in this basin, as well as globally. Future geochemical modeling studies are necessary to elucidate the significance of MSiW and MDAC precipitation in the regional and global marine systems.

6 Summary and implications

All four study sites in the southern Ulleung Basin show a shallow SMT depth (< 5 mbsf) and a microbial CH_4 source, regardless of seismic characteristics (chimney structures at Sites 16GH-P3 and 16GH-P4; non-chimney structures at Sites 16GH-P1 and 16GH-P5), which is consistent with many previous investigations in this basin (e.g., Kim et al, 2011; Kim et al., 2012; Choi et al., 2013; Kim et al., 2013). However, pore fluid and sediment characteristics, including MDACs, have similar and/or different aspects at each study site. The highest Cl^- concentration in pore fluids is observed at Site 16GH-P4, which is greater than that of seawater. In addition, δD and $\delta^{18}O$ values are slightly lower at this site compared to the other sites and have a negative correlation with Cl^-. Such characteristics are typical when the fluid related to massive GH formation in the fine sediment layer impacts the fluid chemistry. In contrast, the fluids at other sites predominantly originate from seawater in the Ulleung Basin. We observe 1) high alkalinity around the SMT (> 35 mM), 2) continuous increase in alkalinity with depth, and 3) higher concentrations of K^+, B, Mg^{2+}, and H_4SiO_4 in pore fluids compared to seawater, which is evidence for the ongoing occurrence of MSiW under anoxic conditions at all sites.

The decreasing downcore profile of Ca^{2+} and Sr^{2+} concentrations with relatively high Mg^{2+}/Ca^{2+} ratios (> 6) as alkalinity increases in pore fluids indicates carbonate precipitation within the sediment column at all sites. However, massive MDACs, mainly composed of aragonite and Mg-calcite, have been found at Sites 16GH-P3 and 16GH-P4 (chimney sites) with diverse morphologies and very low $\delta^{13}C_{MDAC}$ values (< -31.3‰). The ongoing occurrence of MSiW and MDAC precipitation in the Ulleung Basin is first documented in this study. Interestingly, $\delta^{13}C_{MDAC}$ values are clearly separated into two groups based on the SMT at Site 16GH-P3; they are lower than -41.6‰ below the SMT while they are higher than -35.0‰ above the SMT. These results mean that HCO_3^- of seawater with a high $\delta^{13}C$ value (~0‰) impacts MDAC precipitation above the SMT, although the chemical properties of microbial CH_4 are critically inherited into MDACs found at both sites. The measured $\delta^{18}O_{MDAC}$ values above the SMT are close to the present-day theoretical equilibrium value of aragonite (~4‰ V-PDB) in this basin, which also supports the influence of seawater on $\delta^{13}C_{MDAC}$ during the MDAC precipitation. However, compared to the calculated theoretical $\delta^{18}O$ value of aragonite, the observed variation of $\delta^{18}O_{MDAC}$ values at Site 16GH-P4 measured below the SMT implies the involvement of other sources. We postulated that the higher $\delta^{18}O_{MDAC}$ value (~5.7‰) above 6.63 mbsf at this site is related to the fluid derived from GH dissociation, whereas the similar $\delta^{18}O_{MDAC}$ value below 6.63 mbsf is associated with fluid from massive GH formation based on our and previous results of pore fluid chemistry in this basin. Future work will need to generalize the correlation between GH behaviors and $\delta^{18}O_{MDAC}$.

The ACM and ACL facies with an abundance of MDACs have been observed at the chimney sites. The LM, BM, and SLM facies, which are the predominant sediment facies of the non-chimney sites, have also been deposited thickly above the ACM and ACL facies at Site 16GH-P4. The U-Th age dating of MDACs reported first in the Ulleung Basin indicates that the upper facies at Site 16GH-P4 was deposited during a younger period (< 20 ka BP) than the facies at Site 16GH-P3 after mound structure formation by the high upward gas flux. Hence, the depositional environment of the ACM and ACL facies probably contains dynamic conditions associated with sediment erosion or collapse in response to gas flux. The chemical properties of pore fluids and MDACs (i.e., higher concentrations of alkalinity, K^+, Mg^{2+}, B, and H_4SiO_4, and lower $\delta^{13}C_{MDAC}$ values than those of seawater) in the southern Ulleung Basin have very unique characteristics compared to other cold seep regions in the continental margin. These properties reflect the complex chemical interactions between fluids and MDACs in response to gas fluxes and the related elements and carbon cycles. Our study provides some important perspectives for the chemical

reactions and elemental cycles in association with the gas flux of this type of cold seep system. Nevertheless, future investigations into both chimney and non-chimney sites within this basin are necessary to better decipher the chemical properties of pore fluids, gases, and MDACs as well as interactions among them and elemental cycles on regional and global scales in response to climate changes throughout geological history.

Data availability statement

The original contributions presented in the study are included in the article/Supplementary Material. Further inquiries can be directed to the corresponding author.

Author contributions

J-HK and M-HP designed and coordinated the study, analyzed the samples, interpreted the data, and led the writing of the manuscript. J-SR, JC, SP, YS, and T-HK analyzed the samples, wrote, and reviewed the manuscript. KJ, B-YY, YJ, and JH wrote and reviewed the draft. All authors contributed to the article and approved the submitted version.

Funding

The author(s) declare financial support was received for the research, authorship, and/or publication of this article. This study was funded by Korea Ministry of Science and ICT (GP2020-006 and GP2021-009), the Korea Ministry of Oceans and Fisheries (20210632), the Korea Ministry of Trade, Industry and Energy (Project No. 20212010200010), and the National Research Foundation of Korea grant supported by the Korea Ministry of Science and ICT (No. NRF-2019R1A2C2085973).

Acknowledgments

We would like to thank the captain and crew of the *R/V Tamhae II* for their help at sea.

Conflict of interest

The authors declare that the research was conducted in the absence of any commercial or financial relationships that could be construed as a potential conflict of interest.

Publisher's note

Supplementary material

The Supplementary Material for this article can be found online at: https://www.frontiersin.org/articles/10.3389/fmars.2023.1156918/full#supplementary-material

References

Alexeev, S. V., and Alexeeva, L. P. (2003). Hydrogeochemistry of the permafrost zone in the central part of the Yakutian diamond-bearing province, Russia. *Hydrogeol. J.* 11, 574–581. doi: 10.1007/s10040-003-0270-8

Aloisi, G., Bouloubassi, I., Heijs, S. K., Pancost, R. D., Pierre, C., Sinninghe Damsté, J. S., et al. (2002). CH_4-consuming microorganisms and the formation of carbonate crusts at cold seeps. *Earth Planet. Sci. Lett.* 203, 195–203. doi: 10.1016/S0012-821X(02)00878-6

Aloisi, G., Pierre, C., Rouchy, J.-M., Foucher, J.-P., and Woodside, J. (2000). Methane-related authigenic carbonates of eastern Mediterranean Sea mud volcanoes and their possible relation to gas hydrate destabilisation. *Earth Planet. Sci. Lett.* 184, 321–338. doi: 10.1016/S0012-821X(00)00322-8

Bahr, A., Pape, T., Bohrmann, G., Mazzini, A., Haeckel, M., Reitz, A., et al. (2007). Authigenic carbonate precipitates from the NE Black Sea: a mineralogical, geochemical, and lipid biomarker study. *Int. J. Earth Sci.* 98, 677–695. doi: 10.1007/s00531-007-0264-1

Bernard, B. B., Brooks, J. M., and Sackett, W. M. (1978). Light hydrocarbons in recent Texas continental shelf and slope sediments. *J. Geophys. Res.* 83, 4053–4061. doi: 10.1029/JC083iC08p04053

Boetius, A., Ravenschlag, K., Schubert, C. J., Rickert, D., Widdel, F., Gieseke, A., et al. (2000). A marine microbial consortium apparently mediating anaerobic oxidation of methane. *Nature* 407, 623–626. doi: 10.1038/35036572

Böttner, C., Haeckel, M., Schmidt, M., Berndt, C., Vielstädte, L., Kutsch, J. A., et al. (2020). Greenhouse gas emissions from marine decommissioned hydrocarbon wells: leakage detection, monitoring and mitigation strategies. *Int. J. Greenhouse Gas Control.* 100, 103119. doi: 10.1016/j.ijggc.2020.103119

Buerk, D., Klaucke, I., Sahling, H., and Weinrebe, W. (2010). Morpho-acoustic variability of cold seeps on the continental slope offshore Nicaragua: Results of fluid flow interaction with sedimentary processes. *Mar. Geol.* 275, 53–65. doi: 10.1016/j.margeo.2010.04.007

Burton, E. A. (1993). Controls on marine carbonate cement mineralogy: review and reassessment. *Chem. Geo.* 105, 163–179. doi: 10.1016/0009-2541(93)90124-2

Campbell, K. A. (2006). Hydrocarbon seep and hydrothermal vent paleoenvironments and paleontology: Past developments and future research directions. *Palaeogeogr. Palaeoclimatol. Palaeoecol.* 232, 362–407. doi: 10.1016/j.palaeo.2005.06.018

Charkin, A. N., Rutgers van der Loeff, M., Shakhova, N. E., Gustafsson, Ö., Dudarev, O. V., Cherepnev, M. S., et al. (2017). Discovery and characterization of submarine groundwater discharge in the Siberian Arctic seas: a case study in the Buor-Khaya Gulf, Laptev Sea. *Cryosphere* 11, 2305–2327. doi: 10.5194/tc-11-2305-2017

Cheng, H., Edwards, R. L., Shen, C.-C., Polyak, V. J., Asmerom, Y., Woodhead, J., et al. (2013). Improvements in ^{230}Th dating, ^{230}Th and ^{234}U half-life values, and U-Th isotopic measurements by multi-collector inductively coupled plasma mass spectrometry. *Earth Planet. Sci. Lett.* 371-372, 82–91. doi: 10.1016/j.epsl.2013.04.006

Choi, J., Kim, J.-H., Torres, M. E., Hong, W.-L., Lee, J.-W., Yi, B.-Y., et al. (2013). Gas origin and migration in the Ulleung Basin, East Sea; Results from the second Ulleung Basin gas hydrate drilling expedition (UBGH2). *Mar. Pet. Geol.* 47, 113–124. doi: 10.1016/j.marpetgeo.2013.05.022

Chough, S. K., Lee, H. J., and Yoon, S. H. (2000). *Marine geology of korean seas. 2nd ed* (Amsterdam: Elsevier).

Colbo, K., Ross, T., Brown, C., and Weber, T. (2014). A review of oceanographic applications of water column data from multibeam echosounders. *Estuar. Coast. Shelf Sci.* 145, 41–56. doi: 10.1016/j.ecss.2014.04.002

Collett, T. S., Riedel, M., Cochran, J. R., Boswell, R., Presley, J., Kumar, P., et al. (2008). *National gas hydrate program (NGHP) expedition 01 initial reports* (New Delhi: Directorate General of Hydrocarbons).

Craig, H. (1961). Isotopic variation in meteoric waters. *Science* 133, 1702–1703. doi: 10.1126/science.133.3465.1702

Crémière, A., Chand, S., Sahy, D., Thorsnes, T., Martma, T., Noble, S. R., et al. (2018). Structural controls on seepage of thermogenic and microbial methane since the last glacial maximum in the Harstad Basin, southwest Barents Sea. *Mar. Petrol. Geol.* 98, 569–581. doi: 10.1016/j.marpetgeo.2018.07.010

Crémière, A., Lepland, A., Chand, S., Sahy, D., Kirsimäe, K., Bau, M., et al. (2016). Fluid source and methane-related diagenetic processes recorded in cold seep carbonates from the Alvheim channel, central North Sea. *Chem. Geol.* 432, 16–33. doi: 10.1016/j.chemgeo.2016.03.019

Dillon, W. P., Nealon, J. W., Taylor, M. H., Lee, M. W., Drury, R. M., and Anton, C. H. (2001). "Seafloor collapse and methane venting associated with gas hydrate on the blake ridge: causes and implications to seafloor stability and methane release," in *Natural gas hydrates: occurrence, distribution, and detection*. Eds. C. K. Paull and W. P. Dillon (Washington, D.C: American Geophysical Union), 211–233. doi: 10.1029/GM124p0211

Edwards, R. L., Chen, J. H., and Wasserburg, G. J. (1987). ^{238}U-^{234}U-^{230}Th-^{232}Th systematics and the precise measurement of time over the past 500,000 years. *Earth Planet. Sci. Lett.* 81, 175–192. doi: 10.1016/0012-821X(87)90154-3

Gorbarenko, S. A., and Southon, J. R. (2000). Detailed Japan Sea paleoceanography during the last 25 kyr: constraints from AMS dating and δ^{18}O of planktonic foraminifera. *Paleogeogr. Paleoclimatol. Paleoecol.* 156, 177–193. doi: 10.1016/S0031-0182(99)00137-6

Greinert, J., Bohrmann, G., and Suess, E. (2001). "Gas hydrate-associated carbonates and methane-venting at Hydrate Ridge: classification, distribution, and origin of authigenic lithologies," in *Natural gas hydrates: occurrence, distribution, and detection*. Eds. C. K. Paull and W. P. Dillon (Washington, D.C: American Geophysical Union), 99–113.

Haacke, R. R., Hyndman, R. D., Park, K.-P., Yoo, D. G., Stoian, I., and Schmidt, U. (2009). Migration and venting of deep gases into the ocean through hydrate-choked chimneys offshore Korea. *Geology* 37, 531–534. doi: 10.1130/G25681A.1

Han, X. Q., Suess, E., Huang, Y. Y., Wu, N. Y., Bohrmann, G., Su, X., et al. (2008). Jiulong methane reef: microbial mediation of seep carbonates in the South China Sea. *Mar. Geol.* 249, 243–256. doi: 10.1016/j.margeo.2007.11.012

Himmler, T., Birgel, D., Bayon, G., Pape, T., Ge, L., Bohrmann, G., et al. (2015). Formation of seep carbonates along the Makran convergent margin, northern Arabian Sea and a molecular and isotopic approach to constrain the carbon isotopic composition of parent methane. *Chem. Geol.* 415, 102–117. doi: 10.1016/j.chemgeo.2015.09.016

Himmler, T., Brinkmann, F., Bohrmann, G., and Peckmann, J. (2011). Corrosion patterns of seep-carbonates from the eastern Mediterranean Sea. *Terra Nova* 23, 206–212. doi: 10.1111/j.1365-3121.2011.01000.x

Hong, W.-L., Torres, M. E., Carroll, J., Crémière, A., Panieri, G., Yao, H., et al. (2017). Seepage from an Arctic shallow marine gas hydrate reservoir is insensitive to momentary ocean warming. *Nat. Commun.* 8, 5745. doi: 10.1038/ncomms15745

Hong, W.-L., Torres, M. E., Kim, J.-H., Choi, J., and Bahk, J.-J. (2014). Towards quantifying the reaction network around the sulfate-methane transition-zone in the Ulleung Basin, East Sea, with a kinetic modeling approach. *Geochim. Cosmochim. Acta* 140, 127–141. doi: 10.1016/j.gca.2014.05.032

Horozal, S., Lee, G. H., Yi, B. Y., Yoo, D. G., Park, K. P., Lee, H. Y., et al. (2009). Seismic indicators of gas hydrate and associated gas in the Ulleung Basin, East Sea (Japan Sea) and implications of heat flows derived from depths of the bottom-simulating reflector. *Mar. Geol.* 258, 126–138. doi: 10.1016/j.margeo.2008.12.004

Hubbard, C. R., Evans, E. H., and Smith, D. K. (1976). The reference intensity ratio, *I/Ic*, for computer simulated powder patterns. *J. Appl. Crystallogr.* 9, 169–174. doi: 10.1107/S0021889876010807

Hubbard, C. R., and Snyder, R. L. (1988). RIR - measurement and use in quantitative XRD. *Powder Diffr.* 3, 74–77. doi: 10.1017/S0885715600013257

Jolivet, L., Shibuya, H., and Fournier, M. (1995). "Paleomagnetic rotations and the Japan Sea opening," in *Active margins and marginal basins of the western pacific*. Eds. B. Taylor and J. Natland (Washington, D.C: American Geophysical Union), 355–369. doi: 10.1029/GM088p0355

Judd, A., and Hovland, M. (2007). *Seabed fluid flow: the impact on geology, biology and the marine environment* (Cambridge: Cambridge University Press). doi: 10.1017/CBO9780511535918

Kastner, M., Elderfield, H., and Martin, J. B. (1991). Fluids in convergent margins - what do we know about their composition, origin, role in diagenesis and importance for oceanic chemical fluxes. *Philos. Trans. R. Soc A.* 335, 243–259. doi: 10.1098/rsta.1991.0045

KIGAM. (2011). *Studies on gas hydrate geology, geochemistry* (Daejeon: KIGAM).

KIGAM. (2016). *Studies on gas hydrate resource assessment and characterization of chimney structures in the Ulleung Basin* (Daejeon: KIGAM).

Kim, J.-H., Hachikubo, A., Kida, M., Minami, H., Lee, D.-H., Jin, Y. K., et al. (2020). Upwarding gas source and postgenetic processes in the shallow sediments from the ARAON Mounds, Chukchi Sea. *J. Nat. Gas Sci. Eng.* 76, 103223. doi: 10.1016/j.jngse.2020.103223

Kim, J.-H., Hong, W.-L., Torres, M. E., Ryu, J.-S., Kang, M.-H., Han, D., et al. (2021). A pulse of meteoric subsurface fluid discharging into the Chukchi Sea during the Early Holocene Thermal Maximum (EHTM). *Geochem. Geophy. Geosy.* 22, e2021GC009750. doi: 10.1029/2021GC009750

Kim, J.-H., Kong, G. S., Ryu, J.-S., and Park, M.-H. (2014). Revisiting the origin of organic matter and depositional environment of sediment in the central Ulleung Basin, East Sea since the late Quaternary. *Quat. Int.* 344, 181–191. doi: 10.1016/j.quaint.2014.07.022

Kim, J.-H., Park, M.-H., Chun, J.-H., and Lee, J. Y. (2011). Molecular and isotopic signatures in sediments and gas hydrate of the central/southwestern Ulleung Basin: high alkalinity escape fuelled by biogenically sourced methane. *Geo-Mar. Lett.* 31, 37–49. doi: 10.1007/s00367010-0214-y

Kim, J.-H., Park, M.-H., Lee, D.-H., Minami, H., Jin, Y.-K., Hachikubo, A., et al. (2022). Impact of high methane flux on the properties of pore fluid and methane-derived authigenic carbonate in the ARAON Mounds, Chukchi Sea. *Front. Mar. Sci.* 9. doi: 10.3389/fmars.2022.944841

Kim, J.-H., Torres, M. E., Choi, J., Bahk, J.-J., Park, M.-H., and Hong, W.-L. (2012). Inferences on gas transport based on molecular and isotopic signatures of gases at acoustic chimneys and background sites in the Ulleung Basin. *Org. Geochem.* 43, 26–38. doi: 10.1016/j.orggeochem.2011.11.004

Kim, J.-H., Torres, M. E., Haley, B. A., Ryu, J.-S., Park, M.-H., Hong, W.-L., et al. (2016). Marine silicate weathering in the anoxic sediment of the Ulleung Basin: Evidence and consequences. *Geochem. Geophy. Geosy.* 17, 3437–3453. doi: 10.1002/2016GC006356

Kim, J.-H., Torres, M. E., Hong, W.-L., Choi, J., Riedel, M., Bahk, J.-J., et al. (2013). Pore fluid chemistry from the second gas hydrate drilling expedition in the Ulleung Basin (UBGH2): source, mechanisms and consequences of fluid freshening in the central part of the Ulleung Basin, East Sea. *Mar. Petrol. Geol.* 47, 99–112. doi: 10.1016/j.marpetgeo.2012.12.011

Kim, J.-M., Kennett, J. P., Park, B.-K., Kim, D. C., Kim, G. Y., and Roark, E. B. (2000). Paleoceanographic change during the last deglaciation, East Sea of Korea. *Paleoceanography* 15, 254–266. doi: 10.1029/1999PA000393

Kim, S.-T., and O'Neil, J. R. (1997). Equilibrium and nonequilibrium oxygen isotope effects in synthetic carbonates. *Geochim. Cosmochim. Acta* 61, 3461–3475. doi: 10.1016/S0016-7037(97)00169-5

Kim, S.-T., O'Neil, J. R., Hillaire-Marcel, C., and Mucci, A. (2007). Oxygen isotope fractionation between synthetic aragonite and water: influence of temperature and Mg^{2+} concentration. *Geochem. Cosmochim. Acta* 71, 4704–4715. doi: 10.1016/j.gca.2007.04.019

Koch, S., Berndt, C., Bialas, J., Haeckel, M., Crutchley, G., Papenberg, C., et al. (2015). Gas-controlled seafloor doming. *Geology* 43, 571–574. doi: 10.1130/G36596.1

Lee, J. H., Baek, Y. S., Ryu, B. J., Riedel, M., and Hyndman, R. D. (2005). A seismic survey to detect natural gas hydrate in the East Sea of Korea. *Mar. Geophys. Res.* 26, 51–59. doi: 10.1007/s11001-005-6975-4

Lee, K. E. (2007). Surface water changes recorded in Late Quaternary marine sediments of the Ulleung Basin, East Sea (Japan Sea). *Palaeogeogr. Palaeoclimatol. Palaeoecol.* 247, 18–31. doi: 10.1016/j.palaeo.2006.11.019

Lee, K. S., Wenner, D. B., and Lee, I. (1999). Using H- and O-isotopic data for estimating the relative contributions of rainy and dry season precipitation to groundwater: example for Cheju Island, Korea. *J. Hydrol.* 222, 65–74. doi: 10.1016/S0022-1694(99)00099-2

Luff, R., Wallmann, K., and Aloisi, G. (2004). Numerical modeling of carbonate crust formation at cold vent sites: significance for fluid and methane budgets and chemosynthetic biological communities. *Earth Planet. Sci. Lett.* 221, 337–353. doi: 10.1016/S0012-821X(04)00107-4

Magalhães, V. H., Pinheiro, L. M., Ivanov, M. K., Kozlova, E., Blinova, V., Kolganova, J., et al. (2012). Formation processes of methane-derived authigenic carbonates from the Gulf of Cadiz. *Sediment. Geol.* 243-244, 155–168. doi: 10.1016/j.sedgeo.2011.10.013

Malinverno, A., Kastner, M., Torres, M. E., and Wortmann, U. G. (2008). Gas hydrate occurrence in a transect across the Cascadia margin from pore water chlorinity and downhill geophysical logs (IODP 311). *J. Geophys. Res.* 113, B08103. doi: 10.1029/2008JB005702

Mazzini, A., Svensen, H., Hovland, M., and Planke, S. (2006). Comparison and implications from strikingly different authigenic carbonates in a Nyegga complex pockmark, G11, Norwegian Sea. *Mar. Geol.* 231, 443–467. doi: 10.1016/j.margeo.2006.05.012

Mazzini, A., Svensen, H. H., Planke, S., Forsberg, C. F., and Tjelta, T. I. (2016). Pockmarks and methanogenic carbonates above the giant Troll gas field in the Norwegian North Sea. *Mar. Geol.* 373, 26–38. doi: 10.1016/j.margeo.2015.12.012

Milkov, A. V., and Etiope, G. (2018). Revised genetic diagrams for natural gases based on a global dataset of >20,000 samples. *Org. Geochem.* 125, 109–120. doi: 10.1016/j.orggeochem.2018.09.002

Naehr, T. H., Eichhubl, P., Orphan, V. J., Hovland, M., Paull, C. K., Ussler, W. III, et al. (2007). Authigenic carbonate formation at hydrocarbon seeps in continental

margin sediments: a comparative study. *Deep-Sea Res. II: Top. Stud. Oceanogr.* 54, 1268–1291. doi: 10.1016/j.dsr2.2007.04.010

Pape, T., Bahr, A., Rethemeyer, J., Kessler, J. D., Sahling, H., Hinrichs, K.-U., et al. (2010). Molecular and isotopic partitioning of low molecular-weight hydrocarbons during migration and gas hydrate precipitation in deposits of a high-flux seepage site. *Chem. Geol.* 269, 350–363. doi: 10.1016/j.chemgeo.2009.10.009

Park, C., Kim, H., and Song, Y. (2018). Mineralogical, micro-textural, and geochemical characteristics for the carbonate rocks of the lower Makgol Formation in Seokgaejae section. *Econ. Environ. Geol.* 51, 323–343. doi: 10.9719/EEG.2018.51.4.323

Park, M.-H., Kim, J.-H., and Kil, Y.-W. (2007). Identification of the late Quaternary tephra layers in the Ulleung Basin of the East Sea (Sea of Japan) using geochemical and statistical methods. *Mar. Geol.* 244, 196–208. doi: 10.1016/j.margeo.2007.06.006

Park, M. H., Kim, J. H., Ryu, B. J., Kim, I. S., and Chang, H. W. (2006). AMS radiocarbon dating of the marine late Pleistocene-Holocene sediment cores from the Ulleung Basin, East/Japan Sea. *Nucl. Instrum. Methods Phy. Res. B* 243, 211–215. doi: 10.1016/j.nimb.2005.08.120

Paull, C. K., Chanton, J. P., Neumann, A. C., Coston, J. A., Martens, C. S., and Showers, W. (1992). Indicators of methane-derived carbonates and chemosynthetic organic carbon deposits; examples from the Florida Escarpment. *Palaios* 7, 361–375. doi: 10.2307/3514822

Paytan, A., Kastner, M., Martin, E. E., Macdougall, J. D., and Herbert, T. (1993). Marine barite as a monitor of seawater strontium isotope composition. *Nature* 366, 445–449. doi: 10.1038/366445a0

Peckmann, J., Reimer, A., Luth, U., Luth, C., Hansen, B., Heinicke, C., et al. (2001). Methane-derived carbonates and authigenic pyrite from the northwestern Black Sea. *Mar. Geol.* 177, 129–150. doi: 10.1016/S0025-3227(01)00128-1

Peckmann, J., and Thiel, V. (2004). Carbon cycling at ancient methane-seeps. *Chem. Geol.* 205, 443–467. doi: 10.1016/j.chemgeo.2003.12.025

Pierre, C., Bayon, G., Blanc-Valleron, M. M., Mascle, J., and Dupré, S. (2014). Authigenic carbonates related to active seepage of methane-rich hot brines at the Cheops mud volcano, Menes caldera (Nile deep-sea fan, eastern Mediterranean Sea). *Geo-Mar. Lett.* 34, 253–267. doi: 10.1007/s00367-014-0362-6

Pierre, C., Demange, J., Blanc-Valleron, M.-M., and Dupréc, S. (2017). Authigenic carbonate mounds from active methane seeps on the southern Aquitaine Shelf (Bay of Biscay, France): Evidence for anaerobic oxidation of biogenic methane and submarine groundwater discharge during formation. *Cont. Shelf Res.* 133, 13–25. doi: 10.1016/j.csr.2016.12.003

Pimmel, A., and Claypool, G. (2001). *Introduction to shipboard organic geochemistry on the JOIDES Resolution. ODP Tech. Note, 30* (College Station, T.X: Ocean Drilling Program).

Riedel, M., Collett, T. S., Malone, M. J.the Expedition 311 Scientists (2006). *Proceedings of the integrated ocean drilling program, vol. 311* (Washington, D.C: Integrated Ocean Drilling Program Management International).

Römer, M., Sahling, H., Pape, T., Ferreira, C. D., Wenzhöfer, F., Boetius, A., et al. (2014). Methane fluxes and carbonate deposits at a cold seep area of the Central Nile Deep Sea Fan, Eastern Mediterranean Sea. *Mar. Geol.* 347, 27–42. doi: 10.1016/j.margeo.2013.10.011

Ruppel, C. D., and Kessler, J. D. (2017). The interaction of climate change and methane hydrates. *Rev. Geophys.* 55, 126–168. doi: 10.1002/2016RG000534

Ryu, B.-J., Riedel, M., Kim, J.-H., Hyndman, R. D., Lee, Y.-J., Chung, B.-H., et al. (2009). Gas hydrates in the western deep-water Ulleung Basin, East Sea of Korea. *Mar. Petrol. Geol.* 26, 1483–1498. doi: 10.1016/j.marpetgeo.2009.02.004

Scholz, F., Hensen, C., Schmidt, M., and Geersen, J. (2013). Submarine weathering of silicate minerals and the extent of pore water freshening at active continental margins. *Geochim. Cosmochim. Acta* 100, 200–216. doi: 10.1016/j.gca.2012.09.043

Sibuet, M., and Olu, K. (1998). Biogeography, biodiversity and fluid dependence of deep-sea cold-seep communities at active and passive margins. *Deep-Sea Res. II: Top. Stud. Oceanogr.* 45, 517–567. doi: 10.1016/S0967-0645(97)00074-X

Solomon, E. A., Spivack, A. J., Kastner, M., Torres, M. E., and Robertson, G. (2014). Gas hydrate distribution and carbon sequestration through coupled microbial methanogenesis and silicate weathering in the Krishna-Godavari Basin, offshore India. *Mar. Petrol. Geol.* 58, 233–253. doi: 10.1016/j.marpetgeo.2014.08.020

Stott, L., Davy, B., Shao, J., Coffin, R., Pecher, I., Neil, H., et al. (2019). CO_2 release from pockmarks on the Chatham rise-bounty trough at the glacial termination. *Paleoceanogr. Paleoclimatol.* 34, 1726–1743. doi: 10.1029/2019pa003674

Suess, E. (2014). Marine cold seeps and their manifestations: geological control, biogeochemical criteria and environmental conditions. *Int. J. Earth Sci.* 103, 1889–1916. doi: 10.1007/s00531-014-1010-0

Tada, R., Irino, T., and Koizumi, I. (1999). Land-ocean linkages over orbital and millennial timescales recorded in late Quaternary sediments of the Japan Sea. *Paleoceanography* 14, 236–247. doi: 10.1029/1998PA900016

Tamaki, K., Suyehiro, K., Allan, J., Ingle, J. C. Jr., and Pisciotto, K. A. (1992). "Tectonic synthesis and implications of Japan Sea," in *Proceedings of the ocean drilling program scientific results*, vol. 127/ 128 . Eds. K. Tamaki, K. Suyehiro, J. Allan and M. McWilliams (College Station, TX: Ocean Drilling Program).

Teichert, B. M. A., Johnson, J. E., Solomon, E. A., Giosan, L., Rose, K., Kocherla, M., et al. (2014). Composition and origin of authigenic carbonates in the Krishna-Godavari and Mahanadi Basins, eastern continental margin of India. *Mar. Petrol. Geol.* 58, 436–460. doi: 10.1016/j.marpetgeo.2014.08.023

Tomaru, H., Torres, M. E., Matsumoto, R., and Borowski, W. (2006). Effect of massive gas hydrate formation on the water isotopic fractionation of the gas hydrate system at Hydrate Ridge, Cascadia margin offshore OR. *Geochem. Geophy. Geosys.* 7, Q10001. doi: 10.1029/2005GC001207

Tong, H., Feng, D., Peckmann, J., Roberts, H. H., Chen, L., Bian, Y., et al. (2019). Environments favoring dolomite formation at cold seeps: A case study from the Gulf of Mexico. *Chem. Geol.* 518, 9–18. doi: 10.1016/j.chemgeo.2019.04.016

Torres, M. E., Hong, W.-L., Solomon, E. A., Milliken, K., Kim, J.-H., Sample, J. C., et al. (2020). Silicate weathering in anoxic marine sediment as a requirement for authigenic carbonate burial. *Earth-Sci. Rev.* 200, 102960. doi: 10.1016/j.earscirev.2019.102960

Torres, M. E., Wallmann, K., Tréhu, A. M., Bohrmann, G., Borowski, W. S., and Tomaru, H. (2004). Gas hydrate growth, methane transport, and chloride enrichment at the southern summit of Hydrate Ridge, Cascadia margin off Oregon. *Earth Planet. Sci. Lett.* 226, 225–241. doi: 10.1016/j.epsl.2004.07.029

UBGH2 Scientists. (2010). *Ulleung basin gas hydrate drilling expedition 2. Preliminary report* (Daejeon: KIGAM).

Wallmann, K., Aloisi, G., Haeckel, M., Tishchenko, P., Pavlova, G., Greinert, J., et al. (2008). Silicate weathering in anoxic marine sediments. *Geochim. Cosmochim. Acta* 72, 2895–2918. doi: 10.1016/j.gca.2008.03.026

Wang, S., Yan, W., Chen, Z., Zhang, N., and Han, C. (2014). Rare earth elements in cold seep carbonates from the southwestern Dongsha area, northern South China Sea. *Mar. Petrol. Geol.* 57, 482–493. doi: 10.1016/j.marpetgeo.2014.06.017

Whiticar, M. J. (1999). Carbon and hydrogen isotope systematics of bacterial formation and oxidation of methane. *Chem. Geol.* 161, 291–314. doi: 10.1016/S0009-2541(99)00092-3

Wu, Q., Hong, J., and Ruan, Z. (2020). Diurnal variations in tropical cyclone intensification. *Geophys. Res. Lett.* 47, e2020GL090397. doi: 10.1029/2020GL0903